Guilherme Santos Rebordão

Bachelor of Science in Micro and Nanotechnology Engineering

Modelling and Development of a Microfluidic Platform for Dielectrophoretic Separation of Polymeric Nanoparticles

Dissertation submitted in partial fulfillment
of the requirements for the degree of

Master of Science in
Micro and Nanotechnology Engineering

Adviser: Prof. Dr. Leonid Gurevich,
Department of Materials and Production,
Aalborg University

Co-adviser: Prof. Dr. Ana G. Silva,
Department of Physics,
Faculty of Sciences and Technology, NOVA University of Lisbon

Examination Committee:

Chairperson: Prof. Dr. Hugo Águas
Rapporteurs: Prof. Dr. Rui Igreja
Prof. Dr. Ana G. Silva

FACULDADE DE CIÊNCIAS E TECNOLOGIA
UNIVERSIDADE NOVA DE LISBOA

November 2019

"You miss 100% of the shots you don't take."
- Wayne Gretzky

Acknowledgements

A long, demanding, but rewarding journey comes to an end with this work. Therefore, I want to take advantage of this section to thank the ones that made it possible, the ones that made it easier to get through, and the ones that came with me along the way.

Regarding the former, I want to start by sincerely thanking Professor Rodrigo Martins and Professor Elvira Fortunato for creating and developing the Micro and Nanotechnology Engineering course into what it is today. Without it, this would not have become a reality. I also want to thank the Department of Materials and Production of Aalborg University for their hospitality and for providing me with everything I needed to complete this work. Of course, a special thank you to my supervisor Professor Leonid, for guiding me in the right direction for the past semester, and for his constant cooperation and willingness to help. Thank you to my co-supervisor, Professor Ana Gomes Silva, for establishing contact with Aalborg University, and for making the communication between the two parties so easy and straight-forward.

Um obrigado enorme à minha família. Primos, avós e tios: estou agradecido por todo o apoio que me deram ao longo desta etapa, mesmo não conseguindo dizer o nome do meu curso duas vezes seguidas sem se enganarem. Mãe e pai: a vocês tenho que agradecer por tudo o que fizeram por mim nos últimos 23 anos. Nunca me faltou nada graças a vocês, e prometo um dia cuidar de vocês como cuidaram de mim. Obrigado por me incentivarem (obrigarem!) a estudar e a mostrarem-me sempre o caminho certo para chegar onde estou hoje. Susana e Stefan: não são família de sangue, mas é como se fossem. Não vos vejo como madrasta e padrasto, vejo-vos sim como amigos – obrigado por tudo. Johanna, Lourenço e Francisco: como vocês sabem, eu fui filho único até aos 10 anos, e a melhor coisa que podia ter acontecido foi vocês terem nascido. Gosto muito de vocês, mas na verdade vocês é que me deviam agradecer me ter como irmão mais velho!

Passando agora a quem embarcou comigo nesta aventura, há coisa de 5 anos. Ao resto do quinteto maravilha – Ricardo, Fred, Bino e Rodas – entramos nisto juntos e saímos juntos, mas não da mesma forma: Ricardo, sais com menos cabelo; Fred, sais com roupas mais coloridas; Bino, sais mais gggagaago; Rodas, sais com mais camisas às riscas. Obrigado aos 4. Matinhus Matex, meu rapper favorito, podes contar sempre comigo para beats e conselhos. Bernas, continua a carregar no W como sempre fizeste. Rolo, ainda acredito que um dia vais conseguir vencer a equipa de floorball da U.Porto sozinho. Obrigado aos velhos do chat – Rodrigues, Bártolo e Saraiva – pelas horas de conversa, conselhos académicos, e mensagens aleatórias. Um shout-out ao Simão, que por vezes até me esqueço que não fazes parte deste curso, mas para nós é como se fizesses. Quero agradecer também ao resto da malta do curso: vamos ser sempre o melhor ano deste curso (não hajam dúvidas), e uma família.

Ao pessoal de Loulé, que alguns já conheço há mais de 15 anos: André, Miguel, Manel, Noddy, Machado, Rui, e claro, Johny (johnyfernandes95 no Instagram, bagaços dêem follow). Mónica, como sabes foram 7 meses difíceis para nós. Obrigado por estares lá para ouvir os meus desabafos e frustrações, e também os meus triunfos e conquistas. Coração azul!

Lastly, I want to thank the friends I made in Aalborg, who made the Portugal-Denmark transition a breeze. David, Nicolai, Mikkel, and Tri: thank you for all the hours spent in the student room, for picking my spirit up when the thesis wasn't going that well, and I know I did the same for you guys. We probably shouldn't have spent that much money on beer…what's wrong with your beer prices, honestly? Hopefully one day you'll come to Portugal and have you jaws drop with our prices. Thank you, Regina, for showing your support throughout the last months, and for all the gossip! Victor and Vibeke, you're of one the nicest couples I've ever met, I genuinely care for you guys. Thank you for the chocolates! Edgars and Nikolaj – I'm happy to say I became friends with you. We might have met each

other through basketball, but our friendship extended itself to night outs, music making, and even geocaching. I wish you all the best. To the rest of my basketball buddies: Ilyan, Frederik, Stjepan, Thang, and Janus: thank you for all the hours spent playing the sport we love, it was a pleasure meeting all of you.

Abstract

The interest surrounding particle separation techniques has increased significantly in the past years, due to its importance in chemical and biological analysis, diagnostics, and food processing, among other areas. Out of the vast array of ways that have been used to separate particles in microfluidics, electric field may be the most common means of separation, given its applicability and versatility. Dielectrophoresis (DEP) occurs in the presence of a non-uniform electric field, and in order to achieve such field, there are two main approaches: by creating an array of metal electrodes along the main channel or by utilizing an electrodeless design. This latter approach is based on creating constrictions on the channel while applying an electric field between the inlet(s) and outlet(s) of the channel.

In this work, done in the Department of Materials and Production of the University of Aalborg, five different models were designed and fabricated on a single fused silica wafer via photolithography, with the ultimate purpose of continuously separating particles with diameters of 20 nm and 150 nm. A detailed overview of the designs and COMSOL simulations, as well as the fabrication techniques and processes can be found throughout the work.

Successful particle separation was achieved in the simulations, at voltages as low as 35 V, with the use of separation channels with a maximum length of 3.1 mm. The fabrication stage of the work was focused on the development of a robust microfabrication process suitable for small, well-defined channels, and its alignment with metal electrodes. Two different fabrication approaches were presented and analysed.

Keywords: Microfluidics; Particle separation; Dielectrophoresis; Photolithography; COMSOL Multiphysics; SU-8; PDMS.

Resumo

O interesse por técnicas de separação de partículas tem aumentado significativamente nos últimos anos, devido à sua importância em análises químicas e biológicas, diagnósticos, processamento alimentar, e outras áreas. De todo o vasto leque de formas que têm sido utilizadas para separar partículas em microfluídica, o campo elétrico é possivelmente o meio mais comum de separação, dada a sua aplicabilidade e versatilidade. Dieletroforese ocorre na presença de um campo elétrico não uniforme e, para atingir esse campo, existem duas abordagens principais: a criação de uma série de elétrodos metálicos ao longo de um canal principal, ou a utilização de um design sem elétrodos. Esta última abordagem baseia-se na criação de constrições no canal enquanto se aplica um campo elétrico entre a(s) entrada(s) e saída(s) do canal.

Neste trabalho, realizado no Departamento de Materiais e Produção da Universidade de Aalborg, cinco modelos diferentes foram projetados e fabricados num único substrato de vidro via fotolitografia, com o objetivo final de separar continuamente partículas com diâmetros de 20 nm e 150 nm. Uma visão geral dos modelos e simulações, bem como das técnicas e processos de fabricação pode ser encontrada ao longo do trabalho.

A separação dos dois tipos de partículas foi alcançada nas simulações, com recurso a tensões tão baixas quanto 35 V, e com o uso de canais de separação com um comprimento máximo de 3,1 mm. A fase de fabricação do trabalho foi focada no desenvolvimento de um processo de microfabricação robusto, adequado para canais bem definidos e de tamanho reduzido, e para o seu alinhamento com elétrodos metálicos. Foram apresentadas e analisadas duas abordagens de fabrico diferentes.

Palavras-chave: Microfluídica, Separação de partículas; Dieletroforese; Fotolitografia; COMSOL Multiphysics; SU-8; PDMS.

Contents

List of Figures

List of Tables

Symbols

a	Particle radius
ε	Permittivity
σ	Electrical conductivity
Re	Reynolds number
Ca	Capillary number
W	Watt

Acronyms

APTES	(3-Aminopropyl)trimethoxysilane
APTMS	(3-Aminopropyl)triethoxysilane
CM	Clausius-Mossotti
DAPI	4′,6-diamidino-2-phenylindole
DEP	Dielectrophoresis
EOF	Electro-osmotic flow
FEM	Finit Element Method
FITC	Fluorescein Isothiocyanate
PDF	Pressure-driven flow
PDMS	Polydimethylsiloxane
PVP	Poly-N-Vinyl-2-Pyrrolidone
RPM	Rotations per minute

1. Motivation and Objectives

Size-based particle separation is an emerging study field, with applications in areas such as healthcare, industry, and research. From the monitoring of harmful bacterial activity to the differentiation of healthy erythrocytes from malaria-infested erythrocytes, the biggest impact of particle separation lies, perhaps, on healthcare [1]. Nanoparticles, although providing numerous applications in pharmacy, biology, and medicine, can also be toxic to organisms, due to their large surface area and reactivity (arised due to the extremely reduced size of the particles) [2]. In recent years, dielectrophoresis (DEP) has been acknowledged as one of the most relevant particle separation techniques. When a nonuniform electric field is created in a microchannel, dielectrophoretic forces are generated, due to the polarizability differences between a particle and a solvent, and particles with different sizes and polarizabilities move at different speeds [3].

Separation of microparticles is becoming widely studied, as there have been reports of successful separation between particles of 5 and 10 μm in diameter, with the use of 600 V [4]. Particles of 5.7 and 15.7 μm in diameter have also been reported to be successfully sorted, with the use of voltages as high as 900 V [3]. Throughout the literature, microparticle separation has received fairly more attention than nanoparticle separation, and successful experiments appear to only materialize with the use of unpractical, relatively high voltages.

The main goal of this work is to design, simulate, and develop devices capable of separating particles of 20 and 150 nm in diameter, with the use of maximum voltages of 35 V. This work may ultimately result in a better understanding of the concepts surrounding particle separation by dielectrophoresis, as well as the fabrication process necessary to achieve it. Due to the complex nature of the production process, several approaches and experiments will be tested, and the respective conclusions will be drawn.

In order to accomplish this goal, several steps must be followed:

1. Design of the models to be tested;

2. Simulations via COMSOL Multiphysics regarding particle separation, flow velocity, and electric field, on each of the models;

3. Fabrication of the final devices with the use of photolithography and soft-lithography techniques.

2. Introduction

2.1. Particle Separation

A typical microfluidic device contains three distinct modules: a sample transportation and preparation module, a separation module and a detection and analysis module. The attention given to particle separation techniques has been rising in recent years, due to its importance in areas such as diagnostics, chemical and biological analyses, food and chemical processing, among others [1]. The relevance of microfluidics in diagnostics cannot be understated, as separation techniques can be used to differentiate living cells from dead cells, and healthy cells from unhealthy cells (epithelial cancer cells or malaria-infected cells), since it has been found that certain diseases can alter the physical properties of cells (properties such as the size of the cell) [5][6]. In the case of epithelial cancer cells, their size is known to be larger in size than healthy cells, and cells infected with malarial parasites are approximately fifty times more rigid than healthy red blood cells, making them unable to circulate in blood vessels, ultimately resulting in blockage of capillaries [7].

Since microfluidic devices require much smaller sample volume, the entire process is made cheaper, faster, and less invasive to patients (when sample extraction is needed). Particle separation techniques can be divided into two categories: passive and active techniques. Passive techniques do not resource to the use of an external force, as they utilize the interaction between flow field, the particles and the channel structure itself. Conversely, active techniques achieve separation by using external forces/fields, offering better performance than passive techniques [1].

Passive techniques include Pinched Flow Fractionation (PFF), Micro Vortex Manipulation, filtration, hydrodynamic filtration, among others. Active techniques consist of Dielectrophoretic separation (DEP), magnetic separation, optical separation, and acoustic separation. Techniques combining both passive and active methods can also be utilized [1].

2.2. Amphiphilic Poly-N-Vinyl-2-Pyrrolidone

Amphiphilic Poly-N-Vinyl-2-Pyrrolidone (Amph-PVP) is a water-soluble polymer with a wide range of applications, from pharmaceutical formulations to electronics and coatings [8]. One of its most promising applications lies in drug delivery, as it has been reported that amphiphilic derivatives of PVP can enhance liposomal membrane stability and construct self-assembled nanocarriers for a broad range of drugs [9]. Amph-PVP's properties such as low toxicity, ability to cutback side toxicity of other substances, and the capability unaltering blood components and their properties, make it a highly biocompatible polymer [9]. In this work, Amph-PVP nanoparticles were synthesized according to [10].

2.3. Dielectrophoresis

Dielectrophoresis (DEP) is, by definition, the motion induced by nonuniform electric fields and is due to a difference of polarizabilities between a particle and a solvent. If an uncharged particle is placed in a non-uniform electric field, it becomes polarized and is therefore subjected to a force – dielectrophoretic force. Conversely, if the field would be uniform, the DEP force affecting the particle

would be zero. This force causes particles to move towards or away from areas of high electric field intensity. The equation for DEP force is stated as:

$$F_{DEP}=2\pi a^3 \varepsilon_m Re(f_{CM})(\nabla |E|^2) \quad (1)$$

Where a is the particle radius, ε_m is the medium permittivity, $Re(f_{CM})$ is the real part of the Clausius-Mossotti (CM) factor, and $\nabla |E|^2$ is the gradient of the square norm of the present electric field. Depending on if the real part of the CM factor is positive or negative, a particle will be attracted/repulsed to/from the areas of high electric field intensity [11]. The CM factor itself is given by:

$$f_{CM}=\frac{\varepsilon_p^*-\varepsilon_m^*}{\varepsilon_p^*+\varepsilon_m^*} \quad (2)$$

$$\varepsilon^* = \varepsilon - \left(\frac{j\sigma}{\omega}\right) \quad (3)$$

Where ε^* represents the complex permittivity, whereas ε and σ illustrate the permittivity and electrical conductivity, respectively, of the particles and the surrounding medium. The angular frequency of the electric field can be described as $\omega = 2\pi f$, and $j = \sqrt{-1}$ since we are dealing with complex numbers [11]. The relation between ε_p^* and ε_m^* is what defines the movement of a particle relative to the gradient of the electric field. If $\varepsilon_p^* > \varepsilon_m^*$ the CM factor is positive, and the DEP is in the same direction as the gradient of the electric field. In this first case, positive DEP is present, which means that particles are pulled towards stronger electric field. On the other hand, if $\varepsilon_p^* < \varepsilon_m^*$, then the CM factor is negative, meaning that the DEP is in the opposite direction as the gradient, resulting in the particle being pulled away from the gradient, and attracted to areas of weaker electric field. This is called negative DEP [1].

Another conclusion that can be taken from this is that $F \sim \nabla E^2$. This dependence of the force with the square of the amplitude of the electric field means that by raising the strength of a DC/AC field, the DEP is also raised. However, when dealing with DC fields, there will always be a competition between DEP and electrophoresis regarding particle motion. This can be avoided by using high-frequency AC fields. This way, electrolysis is suppressed, which can be extremely helpful when working with electrodes [12]. The magnitude of the DEP force is also heavily dependent on particle volume [11].

Like mentioned before, DEP only occurs in the presence of a non-uniform electric field. In order to achieve such field, there are two main approaches: by creating an array of metal electrodes along the main channel or by using electrodeless DEP. This latter approach is based on creating constrictions on the channel while applying an electric field between the inlet(s) and outlet(s) of the channel. It is common practice to construct special structures (such as hurdles or obstacles) made of electrically insulating materials, which aim to disrupt current flow throughout the microchannel [12].

2.4. Microfluidics

2.4.1. Definition of Microfluidics

The microfluidics field can be briefly described as the study of fluids at the submillimeter scale, making use of channels with dimensions of tens to hundreds of micrometers. This emerging technology possesses numerous, well-known advantages such as the ability to utilize small quantities of reagents and samples, high resolution and sensitivity of analysis, low fabrication cost, and short analysis time. When comparing with fluid phenomena at the macroscale, the effect of gravity is largely reduced at the microscale. Contrarily, other forces such as surface tension and capillary force are more prominent [5],[6]. Microfluidic technology is present in a broad range of applications, with molecular analysis, biodefence, microelectronics, and molecular biology being the four main fields of application.

2.4.2. Fluid Flow

Microfluidics, as the name suggests, requires the movement of fluid inside a microchannel or a system of microchannels. For this to occur, there needs to be a mechanism responsible for it. The three main techniques that allow the generation of liquid flow in microchannels are: pressure-driven flow (PDF), electro-osmotic flow (EOF), and flow induced by volume displacement. Pressure-driven flow might be the most common method used in the microfluidics field, mainly due to its simplicity: by applying a given pressure at the inlets of the microfluidic device, fluid flow is induced throughout the microchannels as a result of the pressure difference established between the inlets and the outlets of the device. Therefore, the velocity of the fluid along the microchannels is dictated by this pressure differential, and also by the resistance of the fluid in relation to the walls of the microchannels [15].

The physics regarding the motion of a fluid in a microchannel are governed by the competition of different phenomena and physical effects, and the relative predominance of the different effects can be described by a series of dimensionless numbers. In microfluidics, the Reynolds number (Re) and the Capillary number (Ca), defined in Table 1 are the ones mentioned the most. The Reynolds number relates inertial force with viscous force and is usually small (Re<<1) or moderate (Re<<100), which reflects the prominence of viscous forces over inertial forces, ultimately resulting in laminar flow. The Capillary Number (Ca) describes the ratio of viscous to interfacial stresses. Given that at the microscale the gravitational effect on a fluid is very small, the viscous and capillary forces arise as the most prominent forces [16], [17].

Table 1 - Dimensionless numbers in microfluidics. Adapted from [18].

Symbol	Name	Formula	Physical meaning
Re	Reynolds number	$Re = \frac{\rho u L}{\mu}$	Inertial force/viscous force
Ca	Capillary number	$Ca = \frac{\mu u}{\gamma}$	Viscous force/interfacial stress

In Table 1, ϱ represents fluid density; u, the linear flow speed; L, the characteristic dimension; μ, the dynamic viscosity and γ the surface tension.

2.4.3. Microfabrication

When it comes to microfabrication, photolithography can be described as its workhorse, being the most common and most thoroughly studied process over the past years. The general photolithography process is well known: first, a wafer is coated with photoresist (the types of photoresists will be addressed in the upcoming section). Subsequently, to solidify the photoresist and also to increase its adhesion to the wafer, a baking stage takes place. This is followed by alignment and UV-exposure stage, where a pre-designed pattern is transferred from a mask to the wafer. This can be followed by a post-exposure bake, depending on the photoresist. Afterward, the wafer is developed until all the excess photoresist is removed from the surface of the wafer. The wafer can still be subjected to an additional hard bake stage to improve its stability [18].

However, the process of photolithography possesses flaws and limitations, as it is an expensive method, given the equipment needed. Another disadvantage is the lack of control over surface chemistry, as well as its inapplicability to non-planar substrates [19]. To complement this process, soft lithography is often used, as it constitutes a different approach to the prototyping of different types of micro- and nanoscale structures. Furthermore, it enables the use of curved and flexible substrates, and the low cost associated with the process makes it very attractive. Soft lithography can be described as the family of techniques for fabricating or replicating structures using conformable photomasks, elastomeric stamps, and molds. Hence, it is called "soft" lithography. Not only is it compatible with biological applications (which is a limitation of conventional photolithography) [19], but, as stated above, it is also a cheap and relatively simple production technique, commonly used in areas such as biology, microfluidics, microelectromechanical systems and flexible photonics/electronics [19].

2.4.4. Photoresist

Photoresists are usually made up of three components: a polymer (base resin), a photoactive component (PAC), a casting solvent, and (optionally) a sensitizer, each with its own function. The casting solvent controls the viscosity of the resist, hence defining the layer thickness; the resin acts as a matrix for other components and is responsible for structural and chemical stability of the resist; the PAC undergoes changes upon illumination and is responsible for pattern transfer; the sensitizers can enhance the PAC's sensitivity or shift it to another part of the spectrum [20].

In the case of photolithography, the most relevant property of a photoresist is its tone, which can be positive or negative. If a photoresist is called positive (positive tone), the resist is weakened when it suffers UV exposure (due to the scission or rupture of the polymeric chains), therefore becoming more soluble in the development stage. On the other hand, if the photoresist is of the negative type (negative tone) it becomes stronger when exposed due to random cross-linkage of the polymeric chains, hence becoming less soluble when developed [20]. Throughout this study, two different photoresists were used: SU-8 2100 (MicroChem SU-8 2000 Series 1x500mL) and S813 G2 (Microposit S1800 G2 Series 1x500mL), which are negative and positive photoresists, respectively [20].

2.5. Finite Element Method (FEM)

The Finite Element Method is a numerical method for problem-solving, widely used in engineering and mathematical applications, such as heat transfer, fluid flow, mass transport, and

structural analysis, for example. What separates the FEM from other methods is the partition of a certain domain into simpler subdomains, which are called finite elements. By doing this, the functions (solutions) vary significantly less from element to element. In order to solve these problems, it is necessary to obtain the solution of partial differential equations related to each finite element. The simple equations that model each of these finite elements are then assembled into a larger equation system, solving the entire problem.

3. Methodology

3.1. COMSOL Simulations

A set of five 3D models were designed and tested in COMSOL, a powerful software that makes use of the FEM, in order to analyse the effects of the channel design, the electric field, and the flow velocity on the separation of the Amph-PVP nanoparticles.

3.2. Mask Design

Preceding the fabrication stage, two different photomasks were designed using L-Edit (Tanner Tools EDA). The first design represented the layer for the electrodes, while the second design represented the layer for the microchannels. After the design stage was completed, the photomasks were ordered from Delta Mask (Delta Mask B.V.).

3.3. Production Techniques

For both the electrode and the microchannel layer, standard photolithography procedures were followed, according to the datasheets provided by each of the photoresist manufacturers. The first step in creating the microfluidic devices was fabricating the electrode layer, and for this, a fused silica wafer was used.

3.3.1. Electrodes

In order to clean the wafer, an ultra-sound bath was used, with the wafer in it (submerged in acetone). The cleaning of the wafer took 5 minutes. Afterwards, a spin-coating stage took place (POLOS SPIN150i). The program used was a pre-defined one specifically created for S1813 photoresist, that consisted of 2 steps: a pre-spin at 500 rpm for 15 s, followed by spin at 3000 for 30 s, with acceleration of 1000 rpm/s. The coated wafer was then placed on a hot-plate for a soft-bake stage and was heated at 120 °C for 1 minute. This was followed by exposure in the mask aligner (SUSS MicroTec MA/BA6), with 150 mJ/cm^2 shone through the mask for 6 s. The photoresist was developed using a solution of 100 ml of water and 50 ml of developer (Microposit Developer Concentrate) for 1.5 minutes and was then rinsed with running water for 30 s.

This was followed by an evaporation stage (Polyteknik A/S Cryofox Explorer 600), where Chromium (10nm)/Gold (150 nm) electrodes were deposited by electron beam evaporation, at a rate of 1 Å/s. The Cr layer was used to promote the adhesion of Au to the wafer. To remove the excess photoresist, a lift-off process ensued. The wafer was submerged in remover PG (MicroChem Remover PG) for two days, which resulted in the detachment of the excess photoresist, leaving only the desired pattern.

3.3.2. Microchannels

In order to fabricate the microchannels on the same fused silica wafer, an oxygen plasma treatment (Surface Technology Systems RIE 320) was applied, at approximately 500 mTorr with a process power of 30 W. The wafer containing the Cr/Au electrodes was etched for 60 s, resulting in the elimination of organic compounds and improved adhesion. Subsequently, the wafer was placed in a desiccator for 1 hour, along with a petri dish containing (3-Aminopropyl)trimethoxysilane (APTMS) ((3-Aminopropyl)trimethoxysilane 97% by Sigma-Aldrich). This step allowed for its gas-phase to be reached and gradually deposited on the wafer.

The wafer was then spin-coated with SU-8 2100 using a pre-defined program: pre-spin at 500 rpm for 10 s, with acceleration of 100 rpm/s, followed by spin at 3000 rpm for 30 s, with acceleration of 300 rpm/s. The wafer was then placed on a hot-plate for a soft-bake stage, firstly at 65 ° C for 3 minutes and then at 95 °C for 9 minutes. Following a cool-down stage, the wafer was exposed with 150 mJ/cm^2 through the mask (with the microchannels pattern) for 12.5 s. To reach this exact exposure time, several tests were performed – this will be thoroughly covered in the results section. The post-exposure bake parameters were: 65 °C/2 minutes followed by 95 °C/7 minutes. The wafer was then developed for 7 minutes and finally rinsed with isopropyl alcohol.

Lastly, the wafer was diced (Disco DAD-321 Dicing Saw) resulting in eight samples of 22 mm by 22 mm, which were rinsed with isopropyl alcohol.

3.3.3. Soft-Lithography

Several batches of PDMS were prepared by mixing an elastomer and a curing agent (Sylgard 184 Silicone Elastomer Kit) with a mass ratio of 10:1, before being placed in a desiccator in order to remove air bubbles from the mixture. The batches were then left overnight in an oven at 60 °C, allowing for a good cure and ideal mechanical and optical properties. This was followed by dicing of the PDMS batches in squares with a side length of approximately 20 mm. All PDMS pieces were given an oxygen plasma treatment for 30 s, for adhesion purposes, and were placed in a desiccator for 1 hour, along with a petri dish containing APTMS.

The previously diced squares, containing the electrodes and the microchannels, were then bonded to the PDMS pieces and placed in an oven at 150 °C for 2 hours. After this time period, the oven's temperature was gradually decreased to 30 °C, temperature at which it stayed for 10 hours. Finally, the inlets and outlets of all the devices were punctured with a blunt needle (1.2 mm diameter). A syringe pump (New Era Syringe Pumps, Inc) was used to inject fluid in the devices, and the tubing was secured with the use of Epoxy Glue. After the course of 10 minutes in an oven at 60 °C the glue solidified, as desired. A simplified illustration of the final fabrication process is presented in Figure 1.

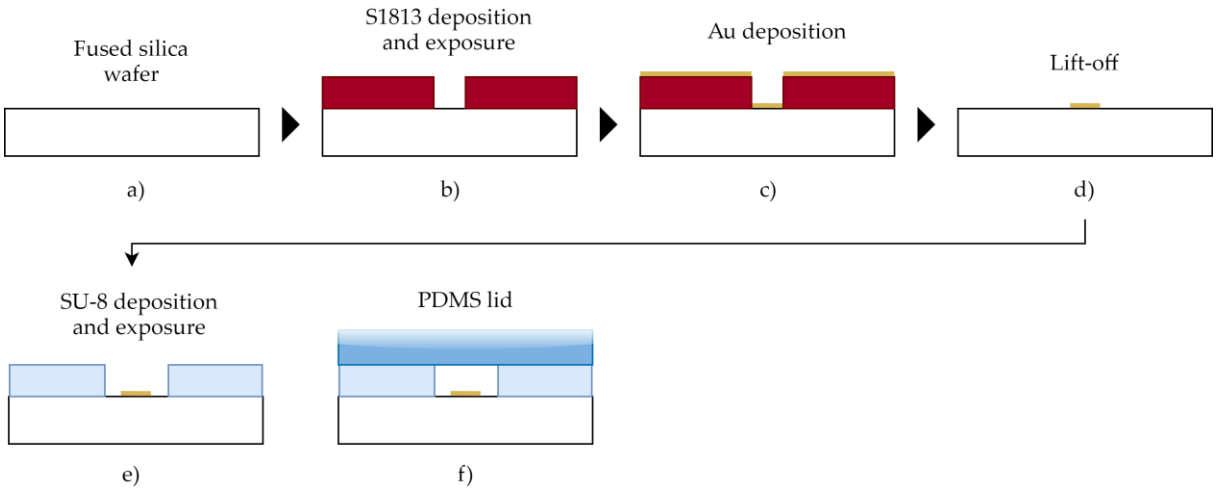

Figure 1 - Simplified schematic of the fabrication process. (a) Starting fused silica wafer; (b) S1813 deposition and exposure; (c) Deposition of the Au electrodes by electron beam evaporation; (d) Lift-off; (e) SU-8 deposition and exposure on the same wafer; (f) Bonding of a PDMS lid.

3.4. Characterization Techniques

To verify the thickness of the deposited photoresist, a profilometer (Ambios Technology XP-2) was utilized. Producing devices with unobstructed microchannels was a major concern throughout the work, so an aqueous solution of fluorescein free acid was used to fill the channels, in order to verify for obstructions. After filled, the devices were inspected with the use of a fluorescence microscope (Zeiss Axioskop 2 Plus).

Two different microscopes were used to analyse the different structures of the final devices: Leica DMI3000 M and Olympus IX71 Inverted Fluorescence Microscope.

4. Results and Discussion

All the results obtained throughout this work will be presented and discussed in this chapter. The different designs and nomenclatures of the models are going to be addressed in the first section, followed by COMSOL simulations. After achieving the final designs, the photomasks for the fabrication process were designed via L-Edit and are here presented as well. In the device fabrication stage, different approaches were tested in order to attain the best possible results. The outcome of each different path will also be addressed in this chapter.

4.1. Design and Nomenclature

In order to understand the consequences of the channel design on particle separation and electric field, five different models were designed (Figure 2). The common focus among all five models was to create a spatially non-uniform electric field, allowing for DEP to occur. All the models were designed with a height of 100 μm. Three of the models consisted of an array of recesses along the separation channel (each one with different features), and the other two models were designed with the intention of testing curved separation channels. For the sake of simplicity, the chosen nomenclature for the five models was A, B, C, D, and E, in the order seen in Figure 2. Regarding the inlets/outlets, the chosen nomenclature was top, middle (in the case of model C) and bottom inlet/outlet.

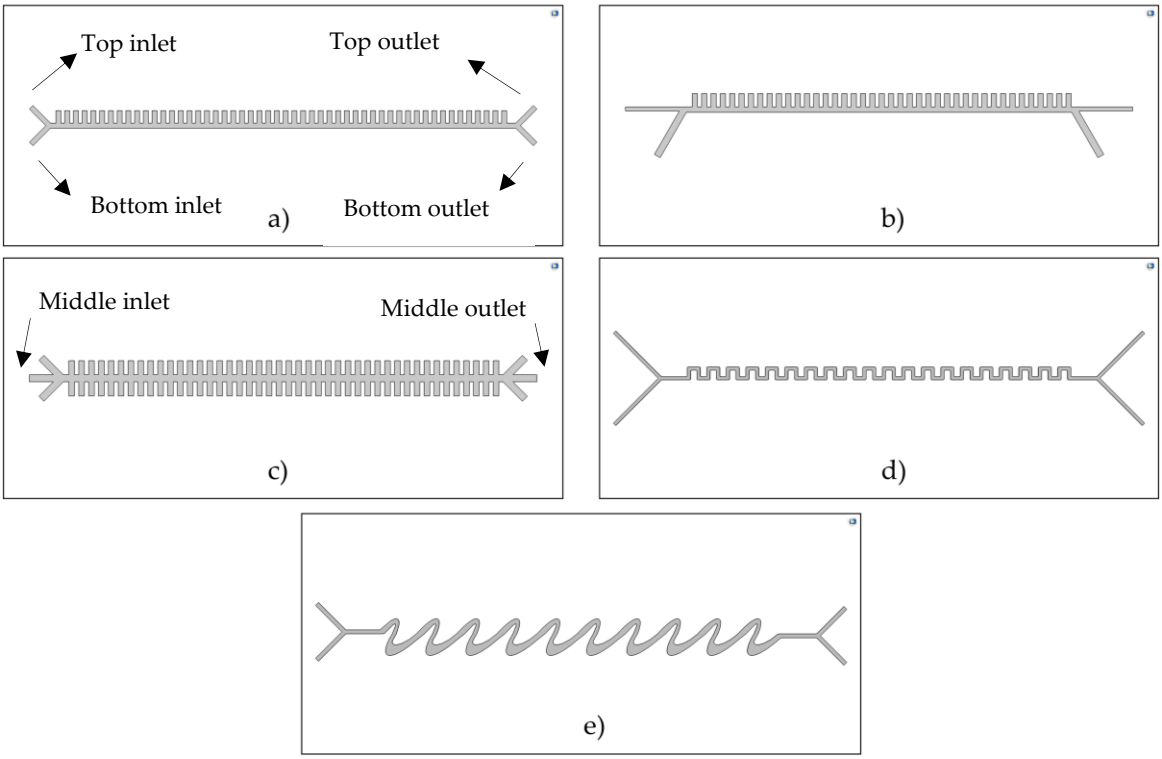

Figure 2 - Design of the five created models: A, B, C, D, and E, respectively.

Regarding models A, B and C, the recesses in the main channel were created with the intention of acting as electrodes (after gold deposition in the fabrication stage). All the recesses are 50 μm wide, 100 μm long and are spaced by 30 μm. A rundown of the measures of the main channel in models A, B and C is presented in Table 2. The first model (A) was adapted from [21], where a similar design was used to simulate the separation of platelets from red blood cells, via COMSOL. This design possesses two inlets and two outlets. Models B and C were based on the same design, though some modifications were made.

Table 2 - Summary of the measures of the main channel in models A, B, and C.

	A	B	C
Channel length	3800 μm	3150 μm	3115 μm
Channel width	50 μm	50 μm	60 μm
Number of recesses	52	41	44 (in each side)

Like stated before, models D and E were created with the intention of testing curved separation channels. Model D was adapted from [22], consisting of an array of 80 perpendicular turns, two inlets, and two outlets. The main channel is 6700 μm long, and 60 μm wide throughout its length. Lastly, model E was created with the purpose of observing the effect of non-perpendicular turns on the channel's electric field. The main channel is 5860 μm long, 70 μm wide in the narrowest curve, and 155 μm in the broadest curve.

4.2. COMSOL Simulation Results

In this section, the COMSOL simulations performed for the five models will be presented and discussed. The most relevant studies for this work are electric potential, electric field strength and particle separation, since the strength of the electric field has a large influence on the dielectrophoretic force, and therefore in particle separation, as shown in equation (1). In all the simulations the medium surrounding the particles is water, and its properties, such as permittivity, density, conductivity, and viscosity, are presented in Appendix A, along with relevant properties of the Amph-PVP nanoparticles, such as density, electrical conductivity, relative permittivity, charge number, and electrophoretic mobility. For the simulations regarding the electric field strength, the original models were shortened, due to the time that it would take to complete the study on the original models. However, the results were just as accurate.

4.2.1. Model A

Like stated before, the channel design in model A was adapted from [21]. However, instead of applying symmetric voltages on the electrodes, a new panel was designed on COMSOL, with the purpose of acting as another electrode. Having the fabrication process in mind, the electrodes were designed on the bottom plane of the COMSOL model. In order to achieve complete separation of the particles, +35 V were applied to the array of electrodes, and -35 V were applied to the added panel electrode. The goal of this approach was to create a difference in electric potential across the width of the main channel. This is displayed in Figure 3 (in figures 3, 4, 6, 8, 10, 12, 32, and 33, where it reads freq(1)=1E5 Hz, should read freq(1)=1×10^5 Hz. This alteration was to possible to perform in the software).

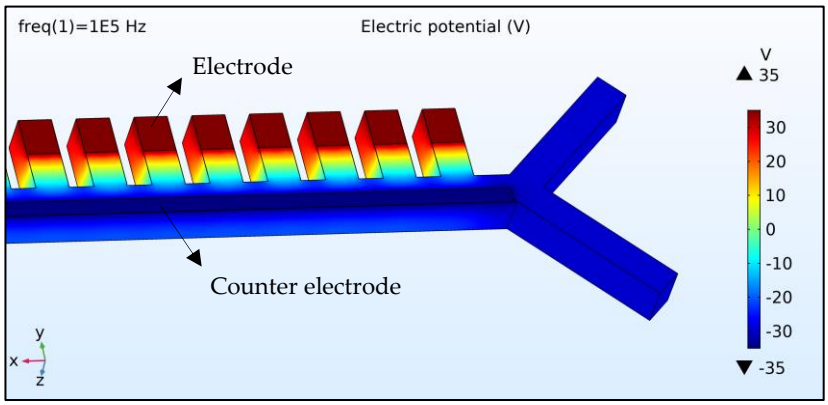

Figure 3 - Bottom plane of model A. +35 V were applied to the electrode array, and -35 V were applied to the electrode panel.

After setting the electric potentials, it was possible to calculate the strength of the electric field throughout the model. As seen in Figure 4, a maximum of 5.52×10^{6} V/m (5.52 V/μm) was reached at the interface of the electrodes in the array.

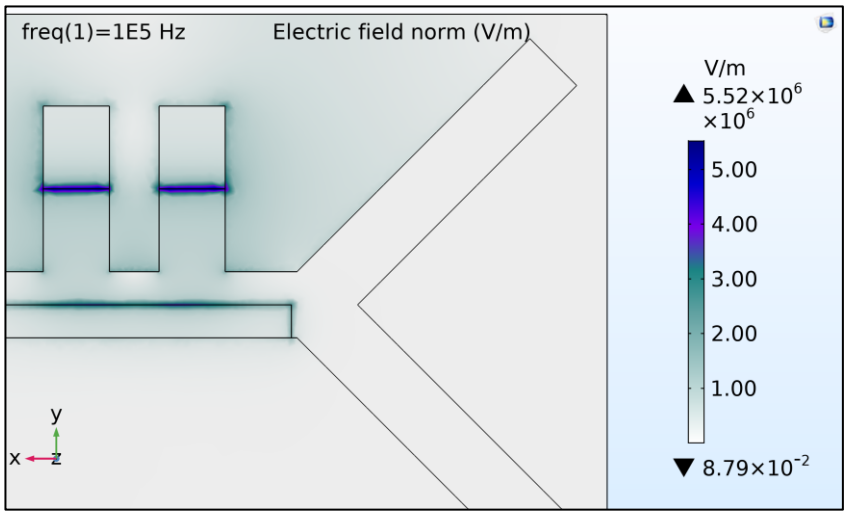

Figure 4 - Electric field strength in model A.

Since the areas of strongest electric field were located at the interface of the array electrodes, the next step was to identify a way of pushing the particle mixture in the direction of the array. With that in mind and taking advantage of the two inlets in the model, different inflow velocities were set at the inlets. At the top inlet, where the particle mixture would be released from in the next study, the inflow velocity was set at 100 μm/s, and at the bottom inlet, the inflow velocity was set at 125 μm/s.

By this stage, everything was set for the particle separation simulation. As mentioned before, the particle mixture containing particles with diameters of 150 nm and 20 nm was released from the top inlet. After 15 s of run time, it was possible to observe a clear separation between both particle types. This is displayed in Figure 5.

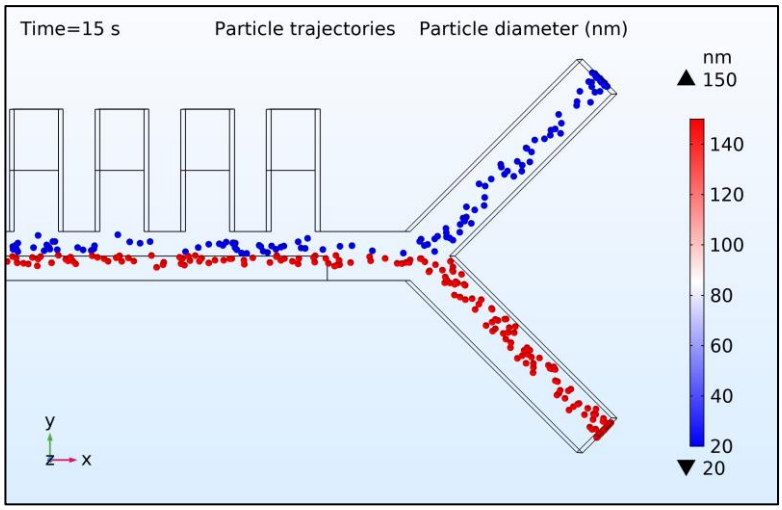

Figure 5 - Successful separation of the particle mixture in model A.

This result is in agreement with equation (1), given that all the particles gradually moved away from the areas of stronger electric field, but the larger particles (150 nm diameter) did it at a faster pace, due to a greater dielectrophoretic force, compared to the smaller particles.

4.2.2. Model B

In this second model, a similar approach was used, but a new inlet/outlet geometry was tested. The top and bottom inlets/outlets were designed to be a continuation of the main channel, while the bottom inlets/outlets remained at an angle of 60° relative to the main channel, like in model A. With this new approach, it was possible to obtain complete separation with +35 V and -35 V as well, and with a smaller device: the channel length needed was 650 µm shorter than in model A, and 11 less recesses were required. With this design, a maximum electric field strength of 2.64×10^6 V/m (2.64 V/µm) was reached at the interface of the electrodes in the array. Both results are displayed in Figure 6.

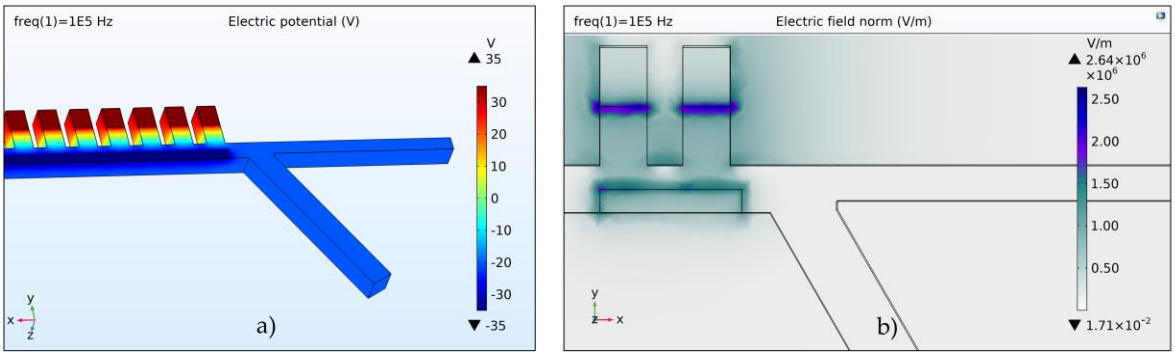

Figure 6 - Electrical simulations in model B: electric potentials (a), and electric field strength (b).

Again, in order to push the particle mixture against the electrode array, the inflow velocities at the inlets were optimized. The inflow velocity at the top inlet was set at 100 µm/s, and at 285 µm/s for the bottom inlet. Just like in model A, the particle mixture was released from the top inlet. Complete

size-based separation was achieved after 15 s of run time, with the 150 nm diameter particles experiencing a larger dielectrophoretic force. This is presented in Figure 7.

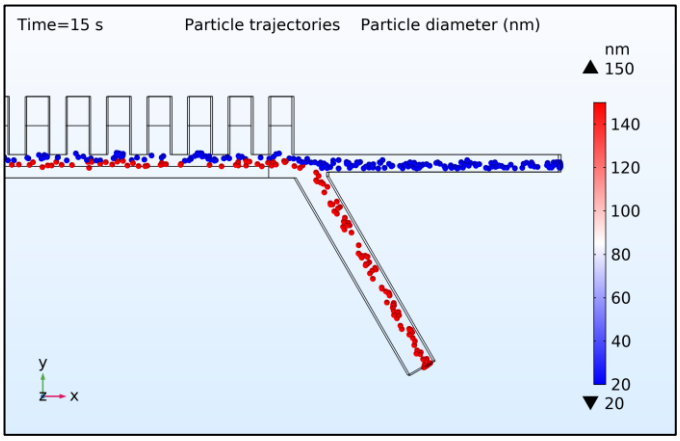

Figure 7 - Successful separation of the particle mixture in model B.

4.2.3. Model C

Two new approaches were tested in model C: rather than having an electrode panel like in the two previous models, the array of electrodes was mirrored; and instead of having two inlets/outlets, three were implemented. The top and bottom inlets/outlets were designed at a 60° angle relative to the main channel, and the middle inlet/outlet was simply a continuation of the main channel. These changes were made with the purpose of not only verifying if there would be any significant changes in the electric field, but also to understand if having more outlets would make it easier for the larger particles to separate from the smaller particles.

With this model, successful particle separation was only possible by applying + 120 V and -120 V to the top and bottom array, respectively (85 V more than in models A and B). This is explained by an overall weaker electric field strength throughout the model (Figure 8). A maximum field strength of 1.68×10^6 V/m (1.68 V/μm) was generated at the electrode interfaces.

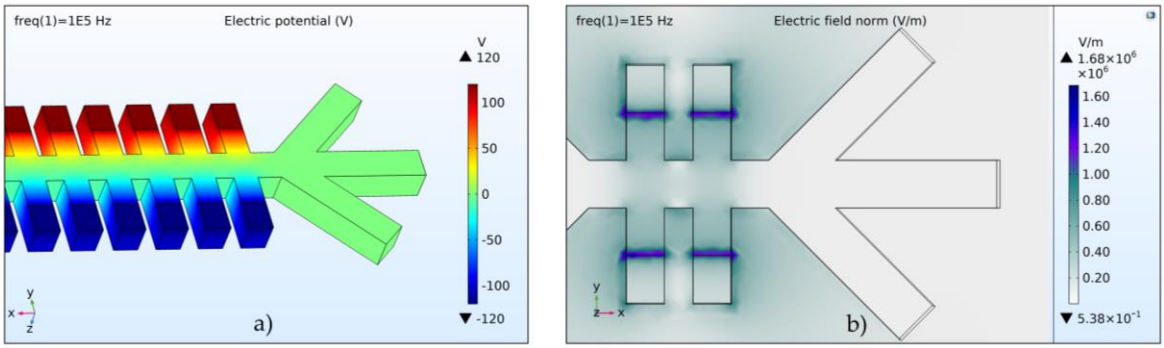

Figure 8 - Electrical simulations in model C: electric potentials (a), and electric field strength (b).

The inflow velocities were set at 100 μm/s, 0 μm/s, and 190 μm/s for the top, middle, and bottom inlets, respectively. Once again, the particles were released from the top inlet and due to the flow distribution, were pushed against the top array. After 45 s of run time, it was possible to see a clear

separation of the mixture. However, due to the new outlet configuration, the small particles flowed in the direction of the top outlet (due to the flow distribution) and the large particles moved along the main channel, in the direction of the middle outlet. This is observed in Figure 9.

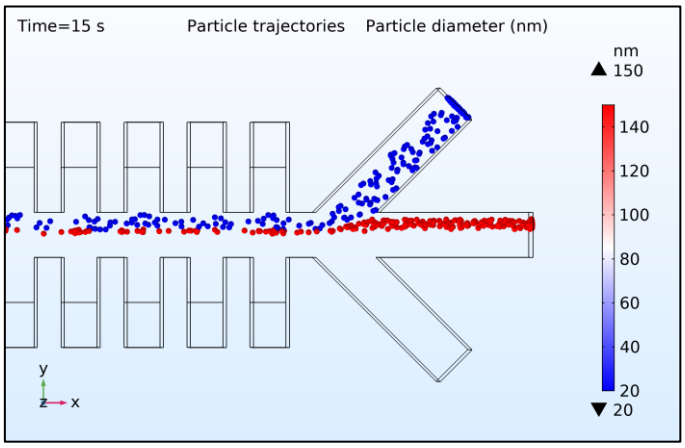

Figure 9 - Successful separation of the particle mixture in model C.

4.2.4. Model D

As it was previously stated, the design of model D was adapted from [22], where a serpentine-shaped microchannel was designed to separate particles based on their size. In this paper, particles with diameters of 2.2 μm and 5 μm were successfully separated, by applying 550 V AC at the inlets, while keeping the outlets grounded. Like expected, by analysing equation (1), higher voltage would be needed to separate particles with sizes in nanometer range. Therefore, instead of 550 V, 700 V AC were applied to the inlets and the outlets were kept grounded.

In agreement with [22], maximum and minimum electric field strength was generated at the inner and outer corners of the design, respectively (Figure 10). With the conditions set in this simulation, the maximum and minimum reached were 1.24×10^5 V/m (0.124 V/μm) and 8.00×10^3 V/m (0.008 V/μm), correspondingly.

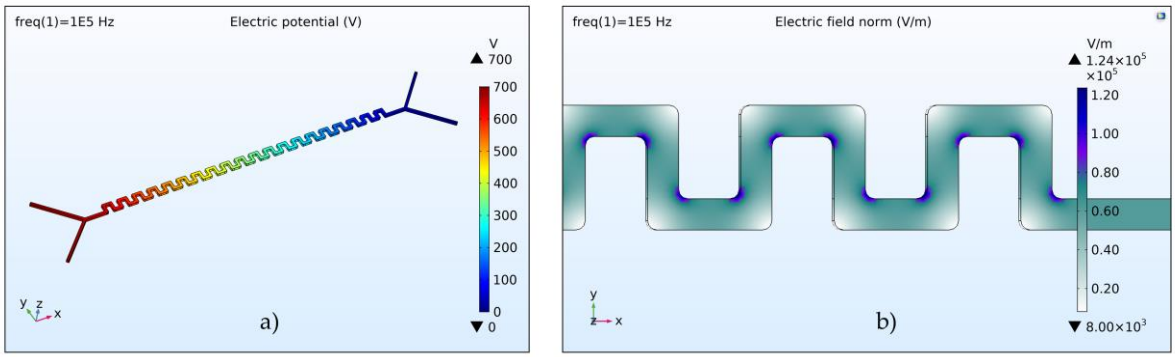

Figure 10 – Electrical simulations in model D: electric potentials (a), and electric field strength (b).

Given that the areas of stronger electric field were located at the inner corners, the inflow velocities were set at 150 μm/s at the top inlet, and at 100 μm/s at the bottom inlet, in order to push the

particles against the first inner corner. In this case, the particle mixture was released from the bottom inlet, and even with 700 V AC applied at the inlets, particle separation was not accomplished (Figure 11). This is mainly due to the weakness of the electric field throughout the design, relatively to the previous models.

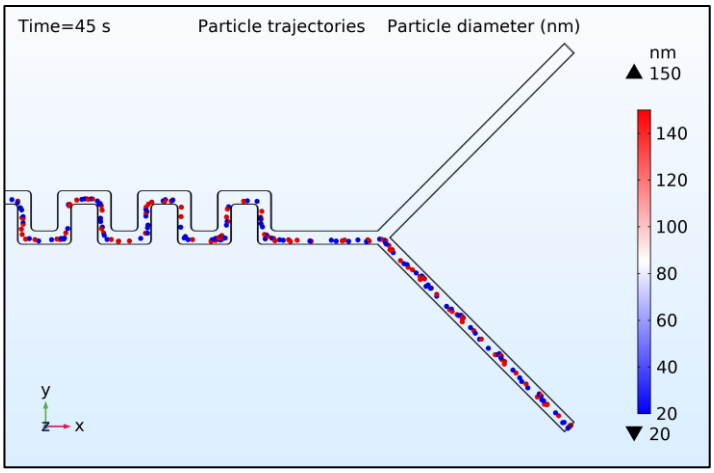

Figure 11 - Unsuccessful separation of the particle mixture in model D.

4.2.5. Model E

With model D, it was possible to investigate what effect do perpendicular turns have on the design's electric field, and therefore in particle separation. The main goal with model E was to verify that same effect but with non-perpendicular turns instead. Thus, the same voltage was applied on the inlets, and the outlets were kept grounded (Figure 12).

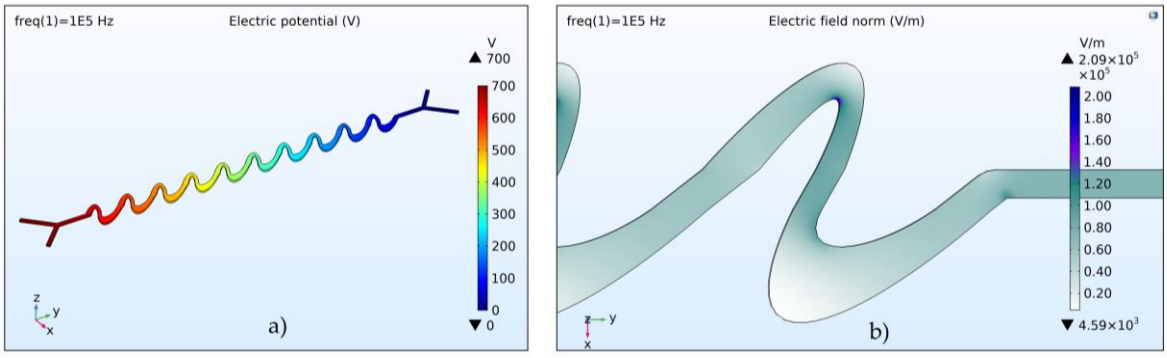

Figure 12 – Electrical simulations in model E: electric potentials (a), and electric field strength (b).

When creating this design, the thought process was to create two different curves – the top and bottom curves – that repeated themselves along the model. Areas of maximum electric field strength were generated at the top curves – 2.09×10^5 V/m (0.209 V/µm). This result was better than the one achieved in model D, but particle separation was unsuccessful, nonetheless. This is displayed in Figure 13.

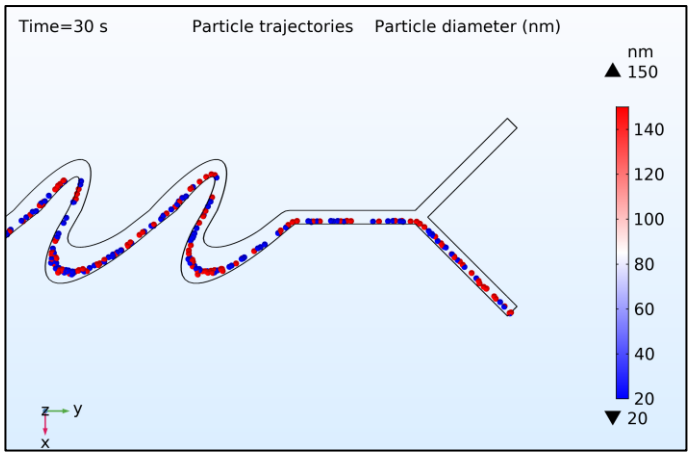

Figure 13 - Unsuccessful separation of the particle mixture in model E.

4.2.6. Discussion of the Simulation Results

Ultimately, the simulation results are in agreement with equation (1) – the DEP force exerted on a particle increases with the strength of the electric field ($\nabla|E|^2$). It is also true that the DEP force can only affect particles in a relatively short range because, depending on the shape and size of the electrodes, there is a gradual decay of the electric field strength [23]. This explains why particle separation was not successful in models D and E (in the simulations).

Particle separation was successful in models A, B, and C, due to the strong areas of electric field that were generated near the electrodes. Like expected, a much higher voltage was needed to separate the particles in model C, due to the weak electric field strength that was generated (in comparison to models A and B). A summary of the obtained results is presented in Table 3, and the exact inflow velocities at the inlets of all the models are presented in Appendix B. Animations of the simulations regarding particle separation can be found in Appendix C.

Table 3 - Summary of the obtained simulation results.

	Model A	Model B	Model C	Model D	Model E
Applied voltage (V)	35/-35	35/-35	120/-120	700/ground	700/ground
Maximum electric field strength (V/m)	5.52×10^6	2.64×10^6	1.68×10^6	1.24×10^5	2.09×10^5
Successful particle separation	Yes	Yes	Yes	No	No

4.3. L-Edit Masks

Having accomplished the final designs, the two masks (for the channels and electrodes) were designed using L-Edit. The masks consisted of eight 22 mm by 22 mm sections: models A, B, C, D, and E, plus a copy of models A, B, and C. This is displayed in Figure 14.

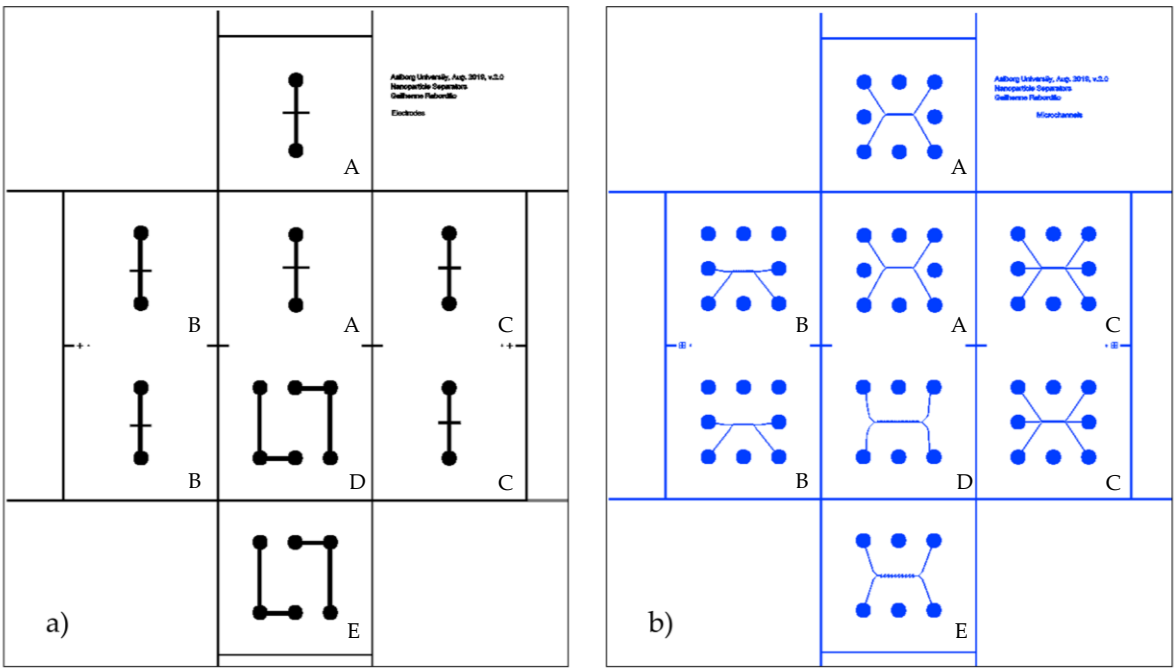

Figure 14 - Masks used in the fabrication stage: (a) electrode mask; (b) channels mask. All the models are labeled.

4.4. Fabrication of the Devices

Until the point of fabricating the final devices, several obstacles had to be overcome. In this section, the problems identified throughout the work will be addressed, along with the solutions that helped overcome them. The main issue throughout the fabrication stage was the bonding process (between PDMS and fused silica) due to limitations of the device. In conventional photolithography and soft-lithography processes, after creating a PDMS mold, a glass or fused silica slide is usually bonded to it without giving too much care regarding alignment. However, in this work the fused silica slide also beared the deposited electrodes, therefore perfect alignment was key. In this section all the chemical products utilized were acquired from Sigma-Aldrich.

4.4.1. Two Wafers vs. One Wafer

In a first attempt, instead of fabricating the channels and the electrodes on the same wafer (like the final devices would come to be produced), two wafers were used - a silicon wafer for the channel layer and a fused silica wafer for the electrode layer. SU-8 2100 photoresist was deposited on the silicon

wafer, and after a complete photolithography process, the microchannels were visible on the silicon wafer.

In this approach, several 3D holders were designed via SolidWorks (by Dassault Systèmes) and printed with the use of Creality LD-001 3D Printer (Figure 15). The printed holders had a square in the middle, tailored for the individual devices (22 mm by 22 mm). PDMS was then spilled on the holders containing the silicon pieces, and after a curing stage, it was successfully peeled off. Finally, the fused silica wafer containing the deposited electrodes was also diced in 22 mm by 22 mm pieces, which were bonded to the PDMS molds via oxygen plasma treatment.

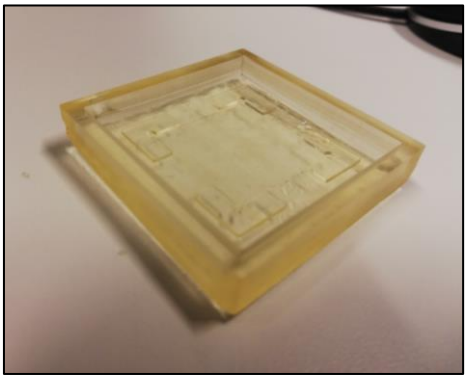

Figure 15 – 3D printed holder.

The bonding was not successful, as only the center of the devices was properly bonded, while the edges were not. This was caused by the walls of the holder, which were necessary to keep the channels and the electrodes aligned. In this approach, the fabricated structures revealed high fidelity to the mask. However, the production stage could not move forward with this issue, due to high probability of leakage in upcoming stages, so a new alternative had to be implemented in order to achieve better bonding. The methodology used in this first approach, as well as the resulting structures, are addressed in Appendices E and F, respectively.

4.4.2. Bonding Experiment

The approach described above presented a challenge: the printed 3D holder allowed for good alignment, but poor bonding due to the of walls of the holder. A solution for this problem was achieved by producing the whole device using a sole wafer, as described in the methodology chapter.

By utilizing only one wafer on the fabrication of the devices, the bonding challenge became simpler, as the 3D holder was no longer needed. Nevertheless, in order to achieve the best bonding possible between SU-8 and PDMS, a bonding experiment was executed, based on [24]. Two PDMS samples of approximately 20 mm by 20 mm were dipped in (3-Aminopropyl)trimethoxysilane (APTMS) and 4 other PDMS samples with the same dimensions were dipped in (3-Aminopropyl)triethoxysilane (APTES). All the 6 PDMS samples were given an oxygen plasma treatment: 3 of the samples were given a 30 s treatment and the other 3 were given a 60 s treatment. Before bonding each of the samples to 22 mm by 22 mm SU-8 coated fused silica chips, two of the chips were also given an oxygen plasma treatment – one for 30 s, and the other for 60 s. This setup is shown in Figure 16, and the results are presented in Table 4.

Figure 16 - Setup of the bonding test between PDMS and SU-8 coated silica. M represents APTMS dipping; E represents APTES dipping; p represents treatment of SU-8.

Table 4 – Outcome of the bonding experiment. PDMS treated with oxygen plasma for 30 s showed the best results out of the six samples, both in bonding to SU-8 and in PDMS transparency.

	30 s treatment	60 s treatment
APTMS	Good bonding Good transparency	Good bonding Average transparency
APTES	Average bonding Good transparency	Average bonding Average transparency
APTES, plasma-treated SU-8	Average bonding Good transparency	Average bonding Average transparency

With this experiment, it was clear that utilizing APTMS-dipping offered better results than APTES-dipping. Across all six PDMS samples, oxygen plasma treatment for 30 s revealed slightly better PDMS transparency, as well as bonding strength. Regarding the oxygen plasma treatment of SU-8, no clear improvement was observed. With this outcome in mind, from this point forward all the bonding steps were made using oxygen plasma treatment for 30 s and dipping in APTMS.

4.4.3. Channel Height

One of the obstacles encountered in this one wafer approach was the channel height. In order to achieve a height of 100 μm, SU-8 2100 was utilized first, and standard procedure was followed according to the SU-8 2100 datasheet. When verifying the channel height with the profilometer, the result was different than expected, as the channels were produced with a height of 154 μm (Figure 17).

One possible explanation for this is the fact that the SU-8 2100 photoresist was past its expiration date, which was noticed only after usage. This may cause the photoresists properties to become suboptimal.

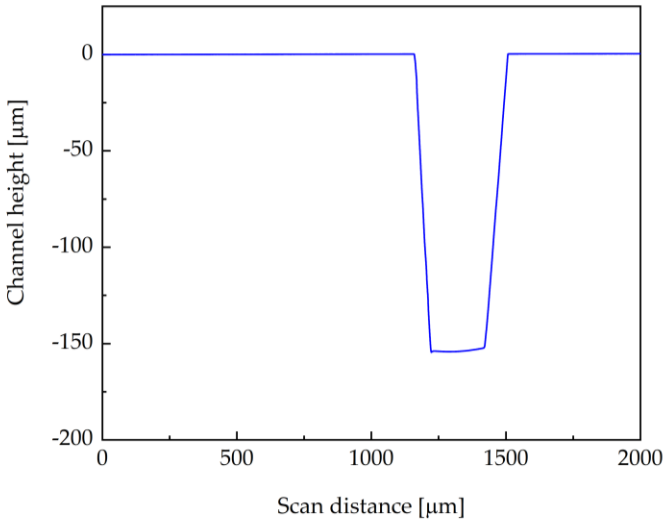

Figure 17 - Channel height using SU-8 2100 photoresist. The scan was made across a dicing marker. Exposure time of 15 s.

The height of the channels was not optimal, so the fabrication carried on merely with the purpose of using the wafer for testing. After completing the photolithography stage, and bonding the wafer to PDMS, the inlets and outlets were punctured and the channels were filled with the aqueous solution of fluorescein free acid. After filling, the devices were inspected, as shown in Figure 18 (the blue color is due to the use of a DAPI filter cube, that excites SU-8 and enhances visualization) and Figure 19.

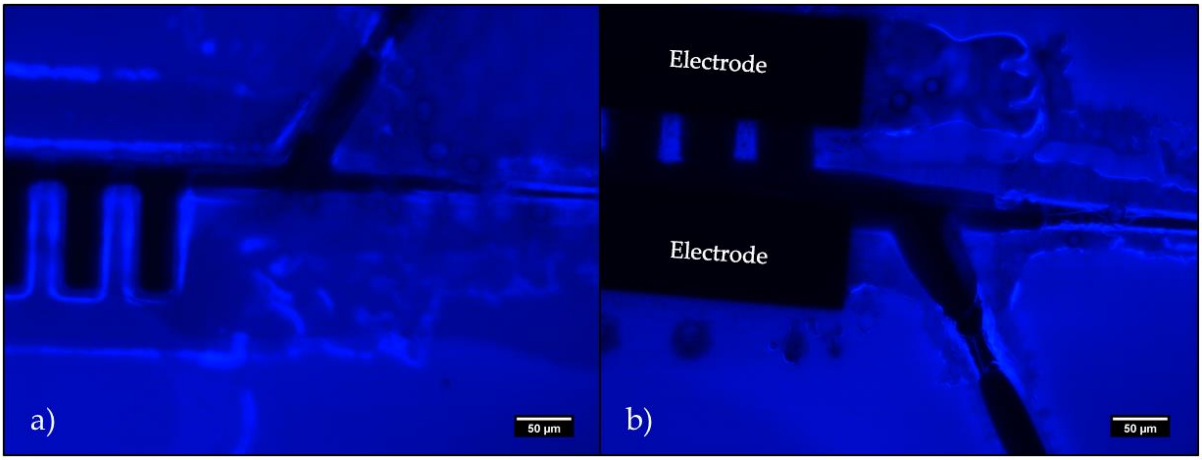

Figure 18 – Obstructions in the channels of model B. Electrodes facing away (a); Electrodes facing the lens (b). Images obtained with the Zeiss Axioskop 2 Plus, with use of a DAPI filter cube.

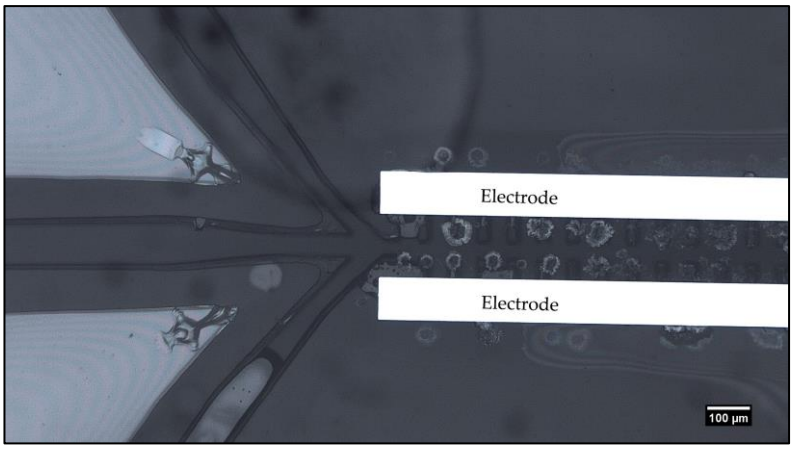

Figure 19 - Blocked inlets of model C. Image obtained with the Leica DMI3000 M.

When observing the images above, it's possible to see that there are several obstructions in the channels: in Figure 18, the outlets of model B are clearly constricted; and in Figure 19 there is noticeable blockage in all the inlets of model C. A likely cause for this issue may be overexposure of the patterned channels, since the resulting SU-8 thickness was not the one in accordance with the datasheet. The longer the wafers are exposed to the radiation, the larger the radiated area is. Hence, overexposure causes the areas beneath the mask to become exposed, and therefore those structures narrower than expected.

To solve this issue, another SU-8 solution had to be used, preferably SU-8 2050. However, SU-8 2050 was not accessible at the time, so a dilution of the SU-8 2100 had to be done. In order to achieve it, a solution was prepared with 61.2 g of SU-8 2100 and 2.3 mL of Cyclopentanone (acquired from Sigma-Aldrich), as advised by Mark Shaw (MicroChem Corp.). After mixing, the solution was placed on a hot plate at 60 °C for 1 hour, and two fused silica wafers were prepared: one for testing purposes (with only the patterned channels), and the other intended for the final devices (with the both the patterned channels and the deposited electrodes).

4.4.4. Exposure Time Experiment

In order to achieve the perfect exposure time on the final devices, an experiment was performed on the testing wafer. After the initial photolithography steps (as described in the methodology chapter), the testing wafer was diced, resulting in eight samples of 22 mm by 22 mm. These samples were then exposed individually using the mask aligner, and for each of the eight samples, a different exposure time was tested. The exposure times tested were 9 s, 10 s, 11 s, 12 s, 13 s, 14 s, 16 s, and 18 s. The exposed samples were named 1, 2, 3, 4, 5, 6, 7, and 8, respectively. Two images were obtained from each sample, regarding a top plane and a bottom plane (Figure 20), to provide a better understanding of the effects of exposure time. In this section, only the images obtained from samples 1, 4, 5, and 8 will be presented. All the images were captured with the use of the Leica DMI3000 M, in bright-field mode. The images obtained from samples 1 and 8 are presented in Figure 21 and Figure 22, respectively.

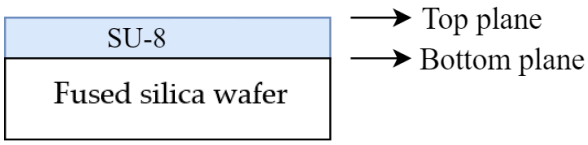

Figure 20 - Schematic of the test wafer, clarifying the top and bottom planes.

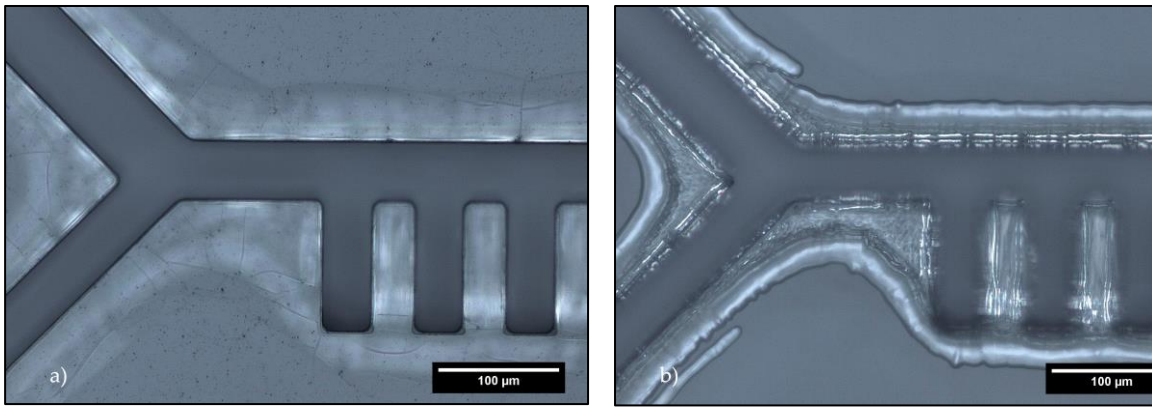

Figure 21 - Sample 1, 9 s of exposure time. Top plane (a) and bottom plane (b).

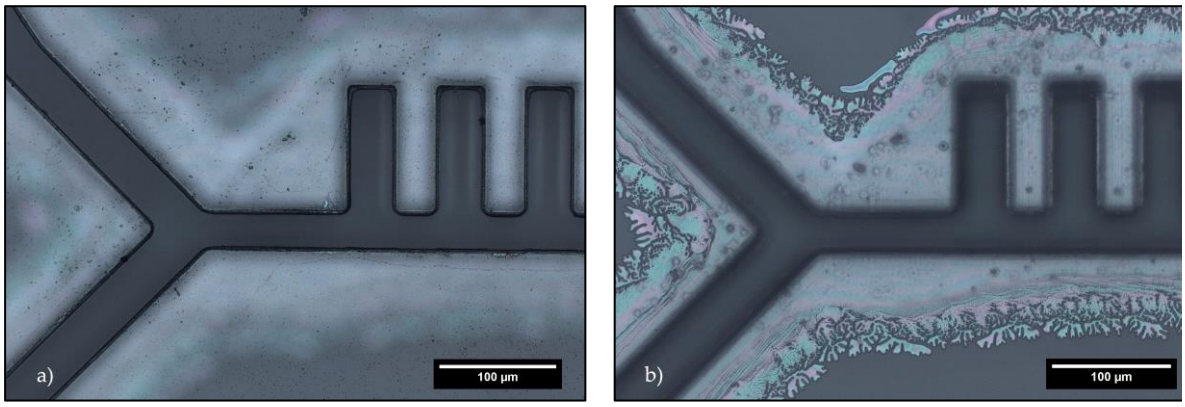

Figure 22 - Sample 8, 18 s of exposure time. Top plane (a) and bottom plane (b).

By observing Figure 21 (b), it is possible to see the consequences of underexposure – SU-8 is cross-linked only to a certain depth, and underetching is observed along the channel near the bottom plane. This is a critical issue in microfluidics, due to the possibility of fluid leakage. In opposition, the effect of overexposure is noticeable in Figure 22 (a) – there is a clear outline surrounding the features, as a result of exposure of the areas beneath the mask. This, like stated before, leads to narrower structures. In order to achieve the most appropriate exposure time, a trade-off needed to happen.

Out of the eight samples, samples 4 (Figure 23) and 5 (Figure 24) exhibited the best balance between undercutting and overexposure.

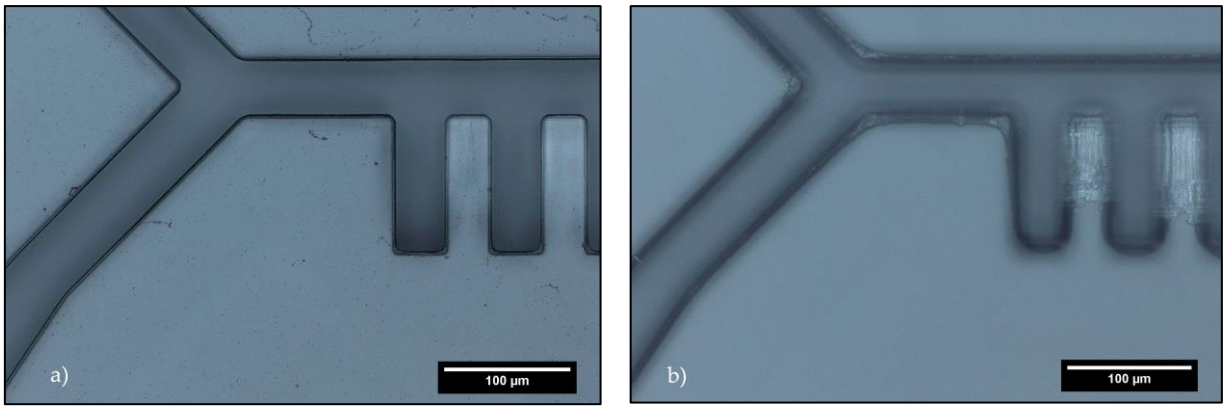

Figure 23 - Sample 4, 12 s of exposure time. Top plane (a) and bottom plane (b).

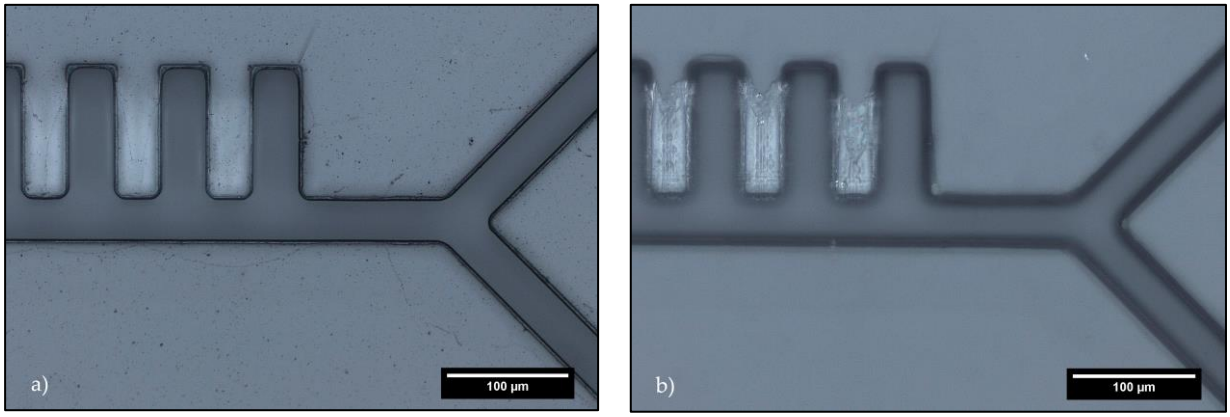

Figure 24 - Sample 5, 13 s of exposure time. Top plane (a) and bottom plane (b).

Finally, a 9th sample was produced, with an exposure time of 12.5 s, halfway between the times used in samples 4 and 5. The images acquired from the 9th and final sample are presented in Figure 25.

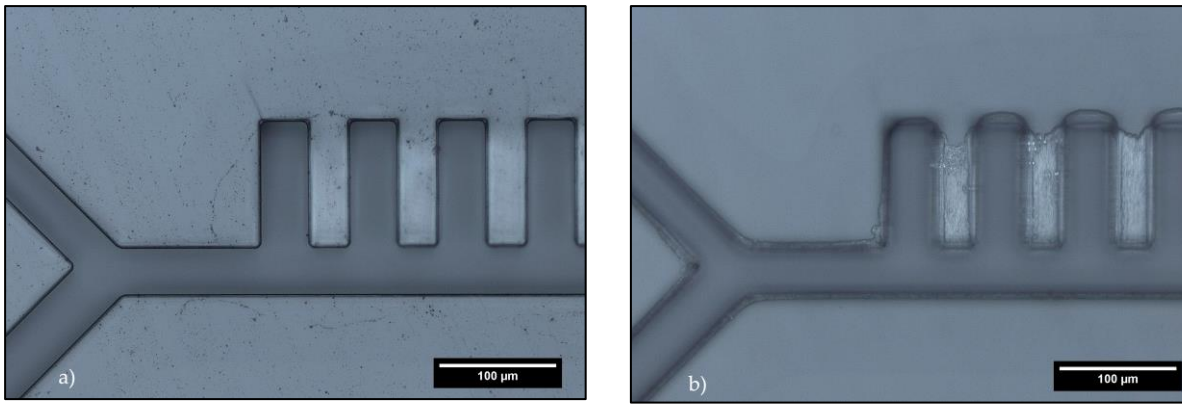

Figure 25 - Sample 9, 12.5 s of exposure time. Top plane (a) and bottom plane (b).

Having identified the adequate exposure time, the final wafer (containing the deposited electrodes) was exposed for 12.5 s in the mask aligner. The remaining steps are described in the methodology chapter. Again, the profilometer was used to verify the height of the channels, this time with the use of the diluted SU-8 2100. The obtained channel height was 74 µm, a more approximate

value to 100 µm than the one obtained with SU-8 2100 photoresist. The slopes of the graph are caused by the width of the measuring tip.

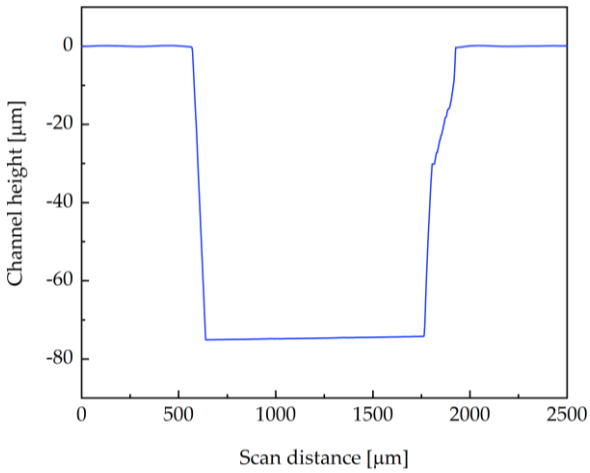

Figure 26 - Channel height using diluted SU-8 2100 photoresist. The scan was made across a dicing marker. Exposure time of 12.5 s.

The final devices were then inspected with the use of the Leica DMI3000 M, prior to the soft-lithography stage. On models A, B, and C, presented in Figure 27. the gold electrodes are clearly visible (white color). Models D and E are electrodeless (Figure 28), hence no electrodes are visible in the images.

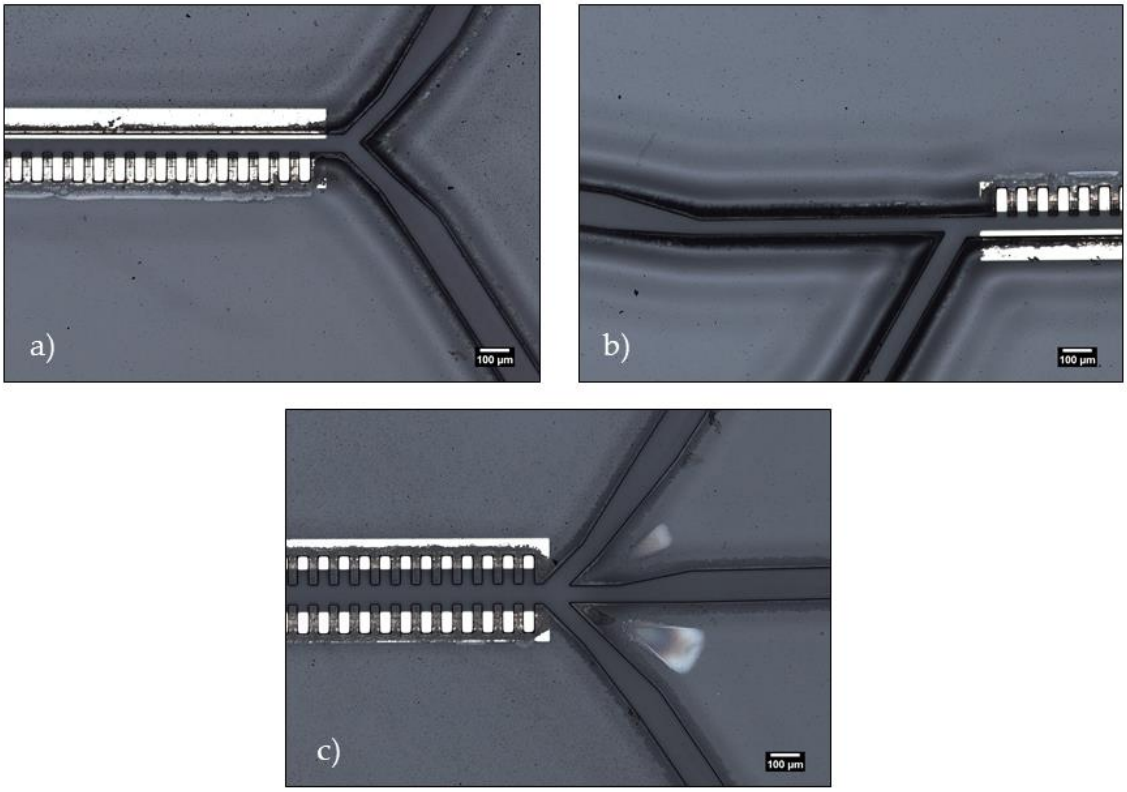

Figure 27 -Models A (a), B (b), and C (c). The white spots between the outlets in (c) may be caused by delamination, derived from stress in the SU-8 layer.

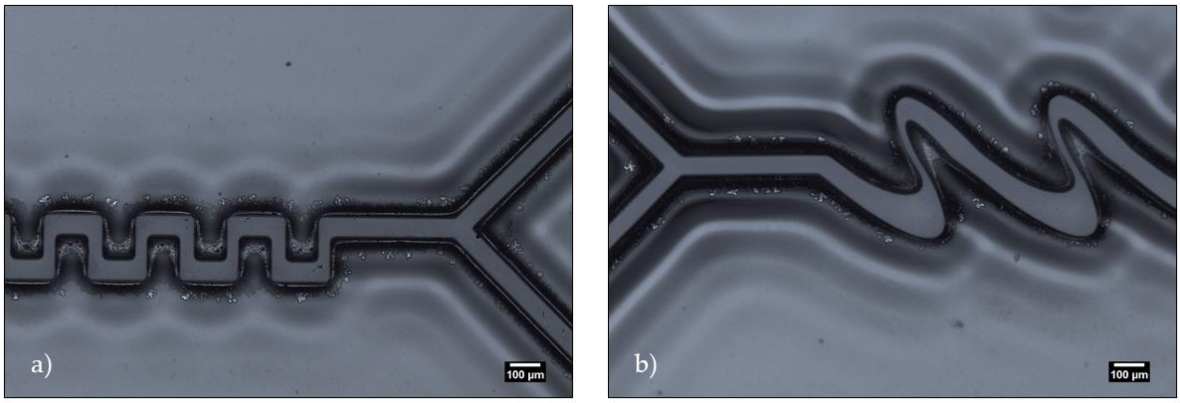

Figure 28 -Models D (a) and E (b).

With 12.5 s of exposure, as expected, the final devices showed good results. No clear structural overcutting was noticeable, and the channel walls appeared to be solid near the bottom plane. Finally, each of the eight samples were bonded to eight PDMS pieces (using the approach discussed in 4.4.2), and everything was set for the device assembly.

4.4.5. Device Assembly

After bonding the samples to PDMS, all the inlets/outlets were punctured, depending on the required inlets/outlets for each model. In order to apply the desired voltage to each design, the correspondent electrode ports were also punctured. All the tubing was placed facing outwards, for visualization purposes. The wires for the electrode ports were secured with the use of Epoxy Glue. The assembly of model C is presented in Figure 29.

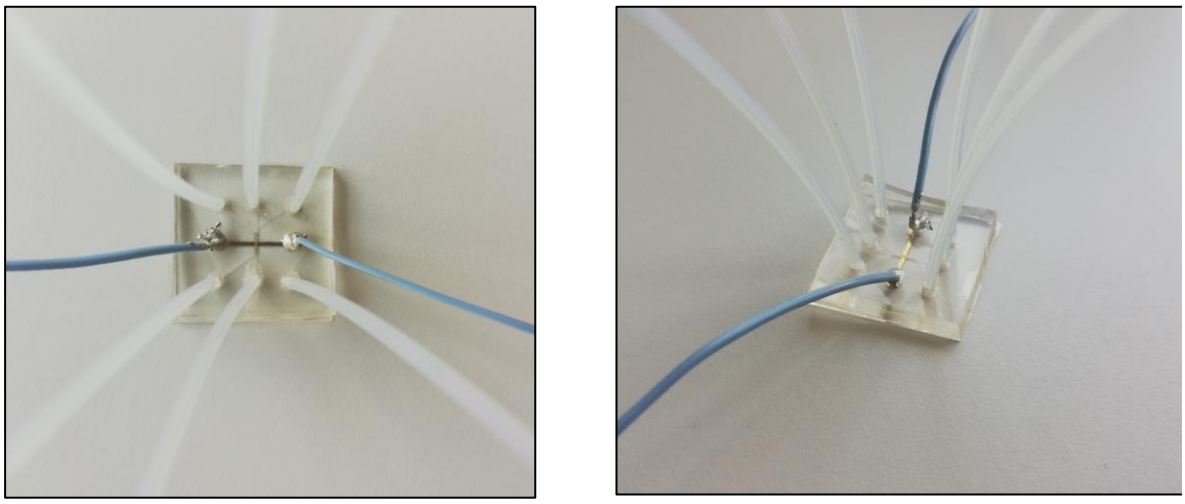

Figure 29 - Model C: assembly of the final device.

After assembling all the devices, some additional images were obtained, in order to check for delamination and misalignment between the different layers of the devices. All images were obtained with the use of the Olympus IX71 Inverted Fluorescence Microscope.

Different visualization approaches were tested in this stage, which can be observed in Figure 30. Images (a) and (b) correspond to models A and B, respectively, and were obtained with the use of a

DAPI fluorescence filter cube, that took advantage of the intrinsic fluorescence of SU-8. Image (c) corresponds to model C and was acquired with the use of a FITC fluorescence filter cube. In this approach the channels were filled with the aqueous solution of fluorescein free acid. Finally, images (d) and (e), that correspond to models D and E, respectively, were again obtained with the use of the FITC fluorescence filter cube, and the channels were also filled with the previously used solution.

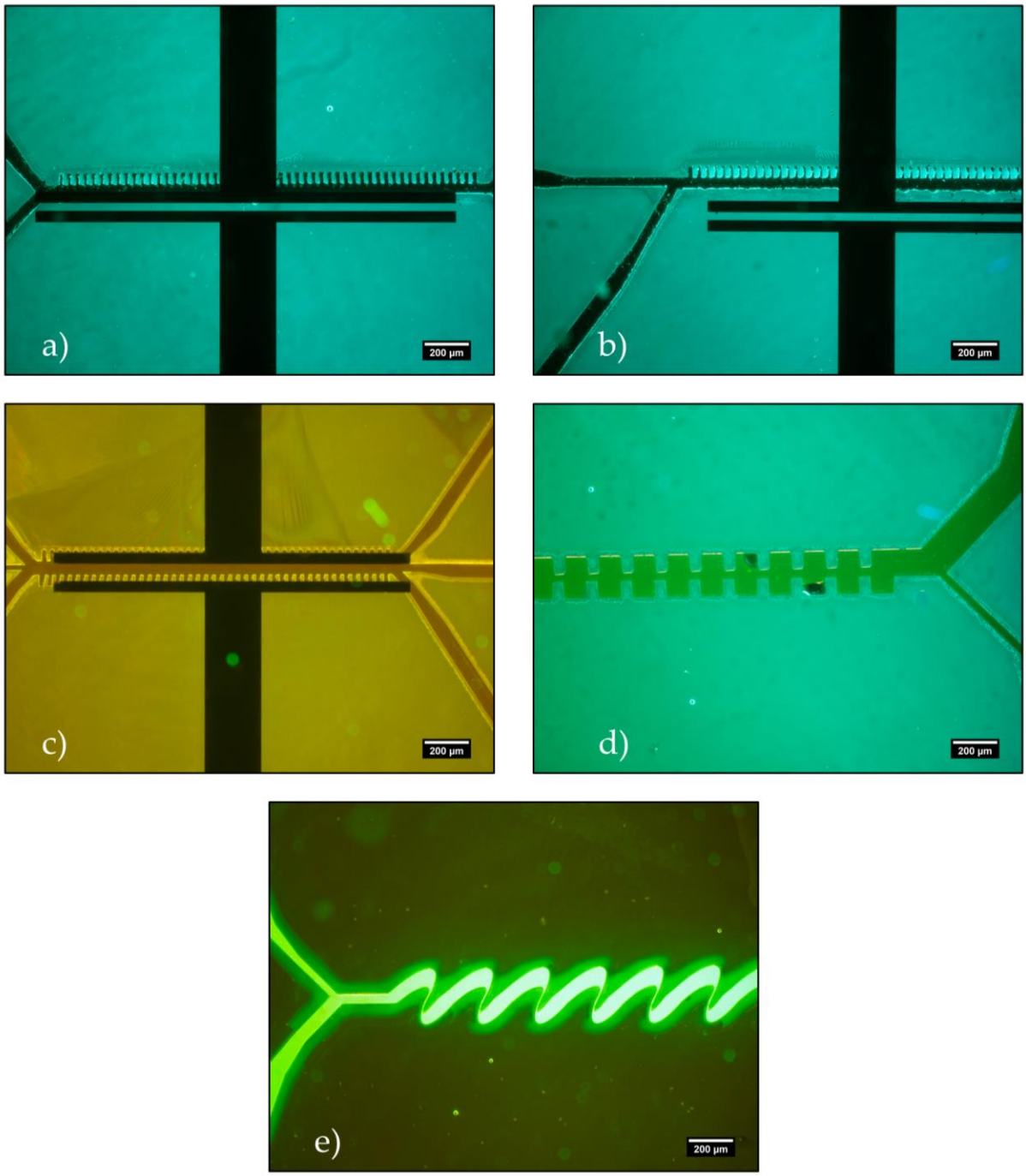

Figure 30 - Device inspection after assembly: model A (a); model B (b); model C (c); model D (d); and model E (e).

By observing the images obtained of models A, B, and C, it is possible to see a clear misalignment between the channels and the electrodes. One possible explanation for this issue is the presence of severe edge bead on the wafer, due to the thick nature of SU-8. With the presence of edge bead, the SU-8 surface is not uniform, which can lead to misalignment when bonding to PDMS. The same complication is seen in model D. Model E presented no alignment issues.

5. Conclusions and Future Perspectives

As stated before, the aim of this work was to model and develop devices capable of separating particles of 20 and 150 nm in diameter, while using a maximum applied voltage of 35 V AC. The obtained results throughout the work were separated into two categories: simulation results and experimental results.

Successful particle separation was achieved via simulation in three of the five created models, and the results were in agreement with the estimates based on interelectrode spacing. Models A and B showed the best results, since the nanoparticles were successfully separated by applying only 35/-35 V AC to the electrode array and electrode panel, respectively. Out of the two, model A offered more potential, since a maximum electric field strength of 5.52×10^6 V/m was generated at the electrode interface, which means that the applied voltage can even be reduced. Model B, as said before, was also successful, with a maximum electric field strength of 2.64×10^6 V/m being generated. In model C, particle separation was successful, but only by applying 120/-120 V AC to the electrode array and electrode panel, respectively, due to the weaker electric field that was generated (1.68×10^6 V/m), when compared to models A and B. Finally, in models D and E it was not possible to achieve separation, as the generated electric field was not strong enough (the acquired values were one order of magnitude lower than the previous three models).

In order to successfully size-sort nanoparticles, three main aspects must be taken into consideration: the applied voltage, the design of the microchannels and electrodes, and the inflow velocities at each of the device inlets. Regarding the applied voltage, the ultimate goal is to generate an electric field strong enough to size-sort the particles, while applying as low voltage as possible, to improve the device's practicality and applicability. This can be accomplished by creating smart channel designs: in the case of models that possess an array of electrodes (models A, B, and C) the width of the electrodes, as well as the space between each electrode (the smaller the distance between electrodes, the steeper gradient can be generated), played a major part in generating areas of strong electric field. Before settling on the final designs, different electrode geometries were tested, and the best results were obtained with 50 μm wide electrodes, spaced by 30 μm. The height of the devices is also crucial: since the electrodes are on the bottom of the device, complete particle separation will not be achieved if the device is too thick, as the particles that flow on top will be less affected by the DEP force. Finally, the inflow velocities at the inlets also play an important role. In order to obtain a stronger DEP force, the particles must be directed towards the regions of stronger electric field (negative DEP), and this was accomplished by adjusting the inflow velocities at each inlet.

After completing the modelling stage of this work, the fabrication process followed. In a first approach to fabricate the devices, two wafers were used – a silicon wafer to form a mold of the channels and a fused silica wafer for the electrode layer – and typical photolithography procedures were used. A critical issue arose concerning the alignment and bonding of the PDMS imprint and the fused silica chips, hence, the production stage could not move forward with this issue, due to high probability of leakage in upcoming stages. A new alternative had to be implemented in order to achieve better bonding.

The final devices were then fabricated using a single fused silica wafer. Both the channels and electrodes were deposited on the same wafer, which helped solve both the alignment and bonding issues described above. A bonding experiment was performed, in order to find the best solution for the bonding between SU-8 and PDMS. The obtained results revealed that the best possible bonding came

from performing an oxygen plasma treatment on PDMS for 30 s and then dipping it in APTMS, before bonding PDMS to the coated wafer.

Another issue that surfaced during the fabrication process was the thickness of the SU-8 channels. When using SU-8 2100, the resulting channel height was 151 μm, which was more than expected – this led to overexposure of the channels in the exposure stage. So, in order to reach optimal channel height, the original SU-8 2100 was diluted with Cyclopentanone, and a channel height of 74 μm was reached (closer to 50 μm, which was the desired height at this stage). To further optimize the exposure stage, another experiment was performed, this time regarding the exposure time of the channels. After testing nine different exposure times, 12.5 s of exposure presented the best results.

The devices were fully assembled, but due to the limited time available, it was not possible to test them for particle separation, since the majority of the time was spent on modelling the devices and optimizing the fabrication process, given the complex structure of these devices. Had the devices been successfully fabricated and made functional, different characterization techniques would have been utilized – Dynamic Light Scattering (DLS) and Nanoparticle Tracking Analysis (NTA) – in order to investigate the sorted nanoparticles.

As for the future, the modelling possibilities for this technology are vast: other designs need to be created, either with or without the use of electrodes, to achieve nanoparticle separation with the use of even lower voltages. To this date, several designs have been proven to successfully separate microparticles, but not nanoparticles: spiral-shaped separation channels [4]; T-shaped separation channels [25]; separation channels with embedded asymmetric electrodes [26]; separation channels with embedded insulating blocks and posts [3],[27]. All of these designs possess great potential and will hopefully be adapted for the separation of nanoparticles in the near future.

In order to make the devices developed in this work apt for testing, edge bead removal in the photolithography stage must certainly be performed. This step will hopefully minimize the misalignment that was noticeable between the S1813 (electrodes) and SU-8 (channels) layers after assembling the devices. When using a single wafer (as was the case in this work), alignment between the electrodes and the channels is of paramount importance – if misalignment occurs, the generated electric field may not affect the nanoparticles.

Ultimately, this work will hopefully lead to a better understanding of the promising technology that is nanoparticle separation by DEP, comprising important aspects such as the theory behind DEP, the effect of channel design on the separation, and fabrication approaches and steps to accomplish such devices.

6. References

[1] P. Sajeesh and A. K. Sen, "Particle separation and sorting in microfluidic devices: A review," *Microfluid. Nanofluidics*, vol. 17, no. 1, pp. 1–52, 2014.

[2] K. Donaldson, V. Stone, C. L. Tran, W. Kreyling, and P. J. A. Borm, "Nanotoxicology," *Occup. Environ. Med.*, pp. 727–728, 2004.

[3] K. H. Kang, Y. Kang, X. Xuan, and D. Li, "Continuous separation of microparticles by size with direct current-dialectrophoresis," *Electrophoresis*, vol. 27, no. 3, pp. 694–702, 2006.

[4] J. Zhu, T. R. J. Tzeng, and X. Xuan, "Continuous dielectrophoretic separation of particles in a spiral microchannel," *Electrophoresis*, vol. 31, no. 8, pp. 1382–1388, 2010.

[5] M. Alshareef *et al.*, "Separation of tumor cells with dielectrophoresis-based microfluidic chip," *Biomicrofluidics*, vol. 7, no. 1, 2013.

[6] S. Suresh *et al.*, "Reprint of: Connections between single-cell biomechanics and human disease states: Gastrointestinal cancer and malaria," *Acta Biomater.*, vol. 23, no. S, pp. S3–S15, 2015.

[7] M. A.G., M. K., Z. M., and R. M., "Plasmodium falciparum," *Trends Parasitol.*, vol. 223, no. December, pp. 7–10, 2018.

[8] P. Knappe, R. Bienert, S. Weidner, and A. F. Thünemann, "Characterization of poly (N -vinyl-2-pyrrolidone) s with broad size distributions," vol. 51, pp. 1723–1727, 2010.

[9] A. L. Luss *et al.*, "Nanosized carriers based on amphiphilic poly-N-vinyl-2-pyrrolidone for intranuclear drug delivery," *Nanomedicine*, vol. 13, no. 7, pp. 703–715, 2018.

[10] P. P. Kulikov, A. N. Kuskov, A. V Goryachaya, A. N. Luss, and M. I. Shtil, "Amphiphilic Poly-N-Vinyl-2-Pyrrolidone : Synthesis , Properties , Nanoparticles," vol. 10, no. 3, pp. 263–268, 2017.

[11] K. Zhao and D. Li, "Tunable Droplet Manipulation and Characterization by ac-DEP," *ACS Appl. Mater. Interfaces*, vol. 10, no. 42, pp. 36572–36581, 2018.

[12] J. Berthier and P. Silberzan, *Microfluidics For Biotechnology*. Journal of Nanobiotechnology, 2009.

[13] G. M. Whitesides, "The origins and the future of microfluidics," *Nature*, vol. 442, no. 7101, pp. 368–373, 2006.

[14] E. K. Sackmann, A. L. Fulton, and D. J. Beebe, "The present and future role of microfluidics in biomedical research," *Nature*, vol. 507, no. 7491, pp. 181–189, 2014.

[15] T. Braschler *et al.*, "A simple pneumatic setup for driving microfluidics," *Lab Chip*, vol. 7, no. 4, pp. 420–422, 2007.

[16] "Formation of bubbles and droplets in microfluidic systems," *Bull. Polish Acad. Sci. Tech. Sci.*, vol. 53, no. 4, pp. 361–372, 2005.

[17] S. Quake and T. Squires, "Microfluidics: Fluid physics at the nanoliter scale," *Rev. Mod. Phys.*, vol. 77, no. 3, pp. 977–1026, 2005.

[18] E. Akçah, K. Nemoto, and R. Uzsoy, "Cycle-time improvements for photolithography process in semiconductor manufacturing," *IEEE Trans. Semicond. Manuf.*, vol. 14, no. 1, pp. 48–56, 2001.

[19] Y. Xia and G. M. Whitesides, "Soft Lithography," *Annu. Rev. Mater. Sci.*, vol. 28, no. 1, pp. 153–184, 1998.

[20] M. Madou, J., *Fundamentals of Microfabrication and Nanotechnology, Volume II: Manufacturing Techniques for Microfabrication and Nanotechnology*. CRC Press, 2011.

[21] COMSOL, "Dielectrophoretic Separation of Platelets from Red Blood Cells," pp. 1–20, 2012.

[22] C. Church, J. Zhu, J. Nieto, G. Keten, E. Ibarra, and X. Xuan, "Continuous particle separation in a serpentine microchannel via negative and positive dielectrophoretic focusing," *J. Micromechanics Microengineering*, vol. 20, no. 6, 2010.

[23] I. Cheng, W. Huang, T. Chen, C. Liu, Y. Lin, and W. Su, "Antibody-Free Isolation of Rare Cancer Cells from Blood based on 3D Lateral Dielectrophoresis," *Lab Chip*, 2015.

[24] Y. Ren, S. Huang, S. Mosser, and M. O. Heuschkel, "A Simple and Reliable PDMS and SU-8 Irreversible Bonding Method and Its Application on a Microfluidic-MEA Device for

Neuroscience Research," pp. 1923–1934, 2015.
[25] H. Jeon, Y. Kim, and G. Lim, "Continuous particle separation using pressure-driven flow-induced miniaturizing free-flow electrophoresis (PDF-induced μ-FFE)," *Sci. Rep.*, vol. 6, no. January, pp. 1–9, 2016.
[26] B. Çetin and D. Li, "Microfluidic Continuous Particle Separation via AC-Dielectrophoresis With 3D Electrodes," no. August 2014, pp. 217–222, 2009.
[27] E. B. Cummings and A. K. Singh, "Dielectrophoresis in microchips containing arrays of insulating posts: Theoretical and experimental results," *Anal. Chem.*, vol. 75, no. 18, pp. 4724–4731, 2003.
[28] M. Viefhues, R. Eichhorn, E. Fredrich, J. Regtmeier, and D. Anselmetti, "Continuous and reversible mixing or demixing of nanoparticles by dielectrophoresis," *Lab Chip*, vol. 12, no. 3, pp. 485–494, 2012.

A. COMSOL Simulation Parameters

Table 5 – COMSOL simulation parameters.

Parameter	Value	Description
f0	100[kHz]	"Frequency of the electric field"
sigma_f	55[mS/m]	"Fluid medium conductivity"
epsilon_f	80	"Fluid relative permittivity"
rho_f	1000[kg/m^3]	"Fluid density"
mu_f	1e-3[Pa*s]	"Fluid dynamic viscosity"
density_PVP	1.2[g/cm^3]	"Particle density"
dp1	20e-9[m]	"Small particle diameter 1"
dp2	150e-9[m]	"Large particle diameter 2"
sigma_PVP	7.42e-8[S/m]	"PVP electrical conductivity"
epsilon_PVP	2.6	"PVP relative permittivity"
chargenum_PVP20	$\frac{3*\pi*mu_{PVP}*mu_f*dp1}{e_{charge}}$	"Small particle charge number"
chargenum_PVP150	$\frac{3*\pi*mu_{PVP}*mu_f*dp2}{e_{charge}}$	"Large particle charge number"
e_charge	1.6e-19[C]	"Electron Charge"
mu_PVP	$\frac{-2*8.84*10^{-12}*78.5*16.4*10^{-3}*1.5}{3*0.8872*10^{-3}}$	"PVP electrophoretic mobility"

B. COMSOL Simulations: Inflow Velocities

The simulated flow profile of each model, at the region of the inlets, is presented in Figure 31. The exact inflow velocities at each inlet is presented in Table 6.

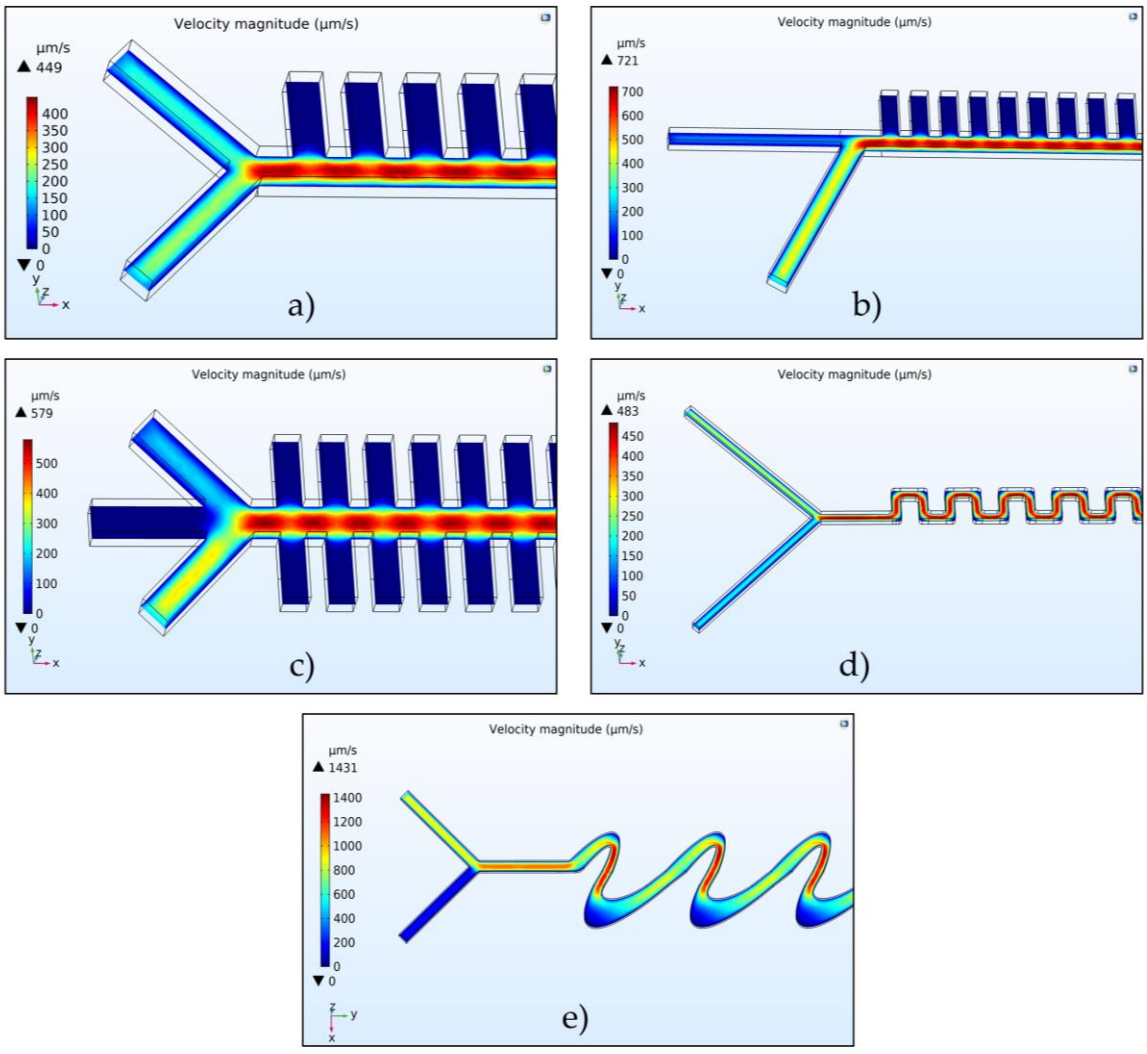

Figure 31 - Flow profile of model A (a), model B (b), model C (c), model D (d), and model E (e).

Table 6 - Inflow velocities of each model.

	Model A	Model B	Model C	Model D	Model E
Top inlet	100 µm/s	100 µm/s	100 µm/s	150 µm/s	150 µm/s
Middle inlet	N/A	N/A	0 µm/s	N/A	N/A
Bottom inlet	125 µm/s	230 µm/s	190 µm/s	100 µm/s	100 µm/s

C. Animations of the Particle Separation Simulations

Below is a QR Code that directs to a Google Drive folder containing animation of the separation simulations.

D. Other Tested Designs

Before reaching the final five models, many other design approaches were tested, some of which will be showcased in this section. One of the first designs to be created consisted in a separation channel with triangular indentations, which is presented in Figure 32. The inlets were grounded, and 500 V AC were applied at the outlets. Maximum electric field strength of 4.42×10^5 V/m (0.442 V/µm) was reached at the vertices of the triangles, which was not enough to size-sort the particles.

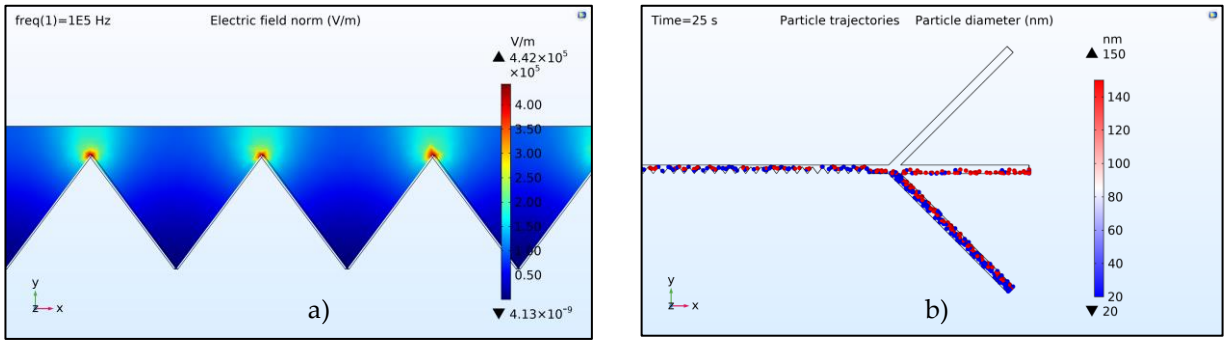

Figure 32 - Testing of triangular indentations. Maximum electric field strength of 4.42×10^5 V/m (0.442 V/µm) was reached at the vertices of the triangles (a), and particle separation was not successful (b).

A design with an array of curved ridges along the channel was also tested (Figure 33), based on [28]. The end of the separation channel was grounded, and 500 V AC were applied at the start of the channel. Maximum electric field strength of 2.96×10^6 V/m (2.96 V/µm) was reached at the top of the ridges, which was also not enough to size-sort the particles. Vertical separation did occur, but not horizontally, like desired.

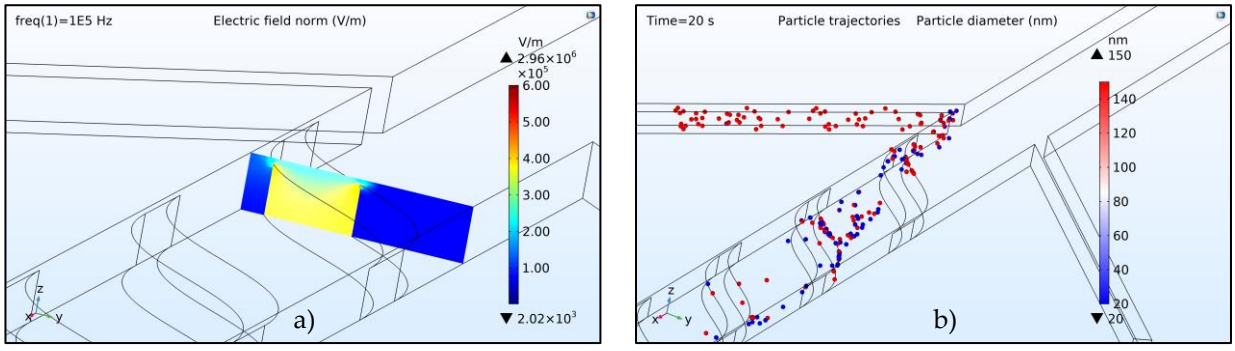

Figure 33 - Testing of ridges. Maximum electric field strength of 2.96×10^6 V/m (2.96 V/µm) was reached at the top of the ridges (a), and particle separation was not successful (b).

E. First Approach: Methodology

To produce the channels, a silicon wafer was washed with acetone, while placed in an ultra-sound bath at room temperature for 5 minutes. For the spin-coating stage and the following steps, typical SU-8 2100 procedure was followed, in accordance with the datasheet. First, there was a pre-spin stage of 500 rpm for 10 s, with acceleration of 100 rpm/s, followed by 2000 rpm for 30 s, with acceleration of 300 rpm/s. The coated wafer was then placed on a hot plate, for a soft-bake stage: 65 °C for 5 minutes followed by 95 °C for 20 minutes, before being cooled-down at room temperature. The wafer was exposed using the mask-aligner, with 290 mJ/cm^2 through the mask for 10 s. This was followed by a post-exposure baking stage, of 65 °C for 20 minutes and 95 °C for 5 minutes. For the development stage, the wafer was submerged in SU-8 developer solution for 10 minutes. After development, the wafer was rinsed again with fresh developer and finally with isopropanol. Lastly, a hard-bake stage took place, consisting of 2 steps: 65 °C for 5 minutes, and 150 °C for 30 minutes. The temperature change between the 2 steps was gradual (10 °C/minute). A cooling stage ensued.

F. First Approach: Resulting Structures

In Figure 34 the fabricated channels that resulted from the first approach are presented. Due to the bonding issue addressed previously these channels were not utilized in the next stages due to the high possibility of fluid leakage, but overall revealed great fidelity to the mask.

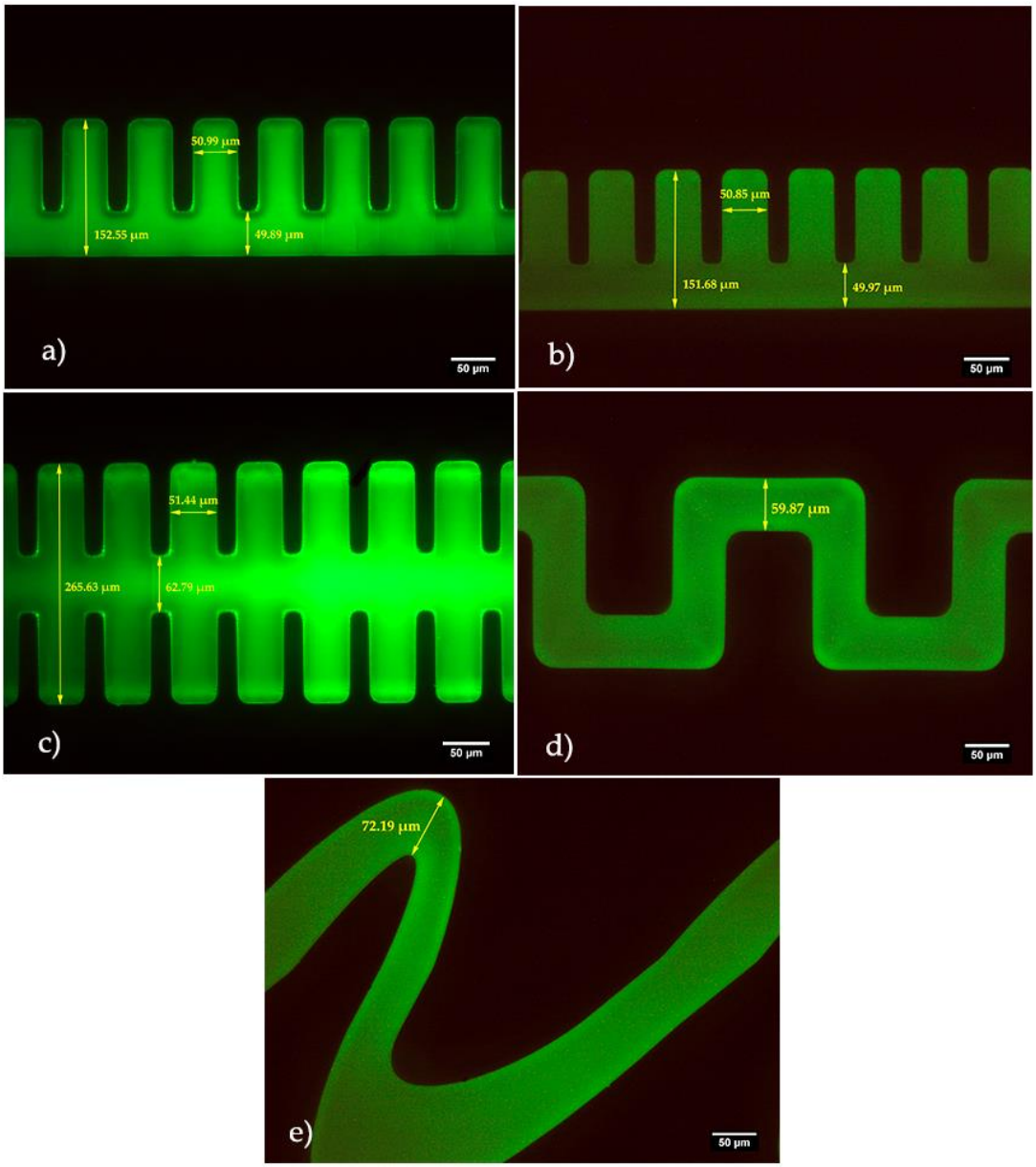

Figure 34 - Resulting SU-8 patterned channels using the first approach (two wafers). Model A (a); Model B (b); Model C (c); Model D (d); Model E (e). Images obtained via Fluorescence Microscopy (Zeiss Axioskop 2 Plus).